Materials and Methods

Data reporting

No statistical methods were used to predetermine sample size. The experiments were not randomized and investigators were not blinded to allocation during experiments and outcome assessment. This study complies with the MINSEQE guidelines for reporting high throughput sequencing experiments.

Ethics statement and sample collection

All animal procedures were performed in compliance with national and international ethical guidelines and regulations for the care and use of laboratory animals, and were approved by the local animal welfare authorities at Heidelberg University Interfaculty Biomedical Research Facility (T-63/16, T-64/17, T-37/18, T-23/19), Vaud Cantonal Veterinary Office (No.2734.0) or Berlin State Office of Health and Social Affairs, LAGeSo (T0198/13). RjOrl:SWISS (RRID:MGI:5603077) time-mated pregnant mice (*Mus musculus*; NCBI:txid10090), litters at postnatal days P0-P14 and adult (P63) mice were purchased from Janvier Labs (France). The adult mice were sacrificed by cervical dislocation, the pups by decapitation. Prenatal samples were collected before noon and are referred to by full completed days *post coitum* (e.g., E10). Gray short-tailed opossums (*Monodelphis domestica*; NCBI:txid13616) were bred in a colony in Museum für Naturkunde Berlin - Leibniz Institute for Evolution and Biodiversity Science (Germany) and sacrificed by an overdose of isoflurane.

We designed our sampling scheme aiming to cover the entire course of cerebellum development in mouse and also considering the previously described periods of greater transcriptional change during early embryonic development and at early postnatal stages (*39*). We sampled at each day during embryonic development (E10-E13), at every second day during fetal development (E15, E17), every 3rd or 4th day during early postnatal development (P0, P4, P7) and at greater intervals during late postnatal development (P14, P63). Opossum cerebella were sampled at two stages, P21 and adult, which based on bulk transcriptomes (*39*) are similar to P4 and adult mouse stages, respectively. Animals of both sexes were

included in the sampling scheme in order to obtain an unbiased dataset that is not over-represented by one sex.

Cerebella were dissected as whole or in 2 halves (table S1). An adult opossum sample enriched for cerebellar white matter was dissected from coronal cerebellum slices. The developmental samples were dissected under a stereomicroscope in ice-cold PBS and most of the meninges were removed. Isthmus and pontine flexure were used as landmarks to locate the cerebellar primordia (fig. S1). All samples were snap-frozen in liquid nitrogen. To determine the sex of the developing animals, tail samples were collected and subjected to PCR genotyping using MyTaq Extract-PCR Kit (Meridian Bioscience) and Y-chromosome-specific primers (mouse: 5'-TCATGAGACTGCCAACCACAG-3' and 5'-CATGACCACCACCACCACCAA-3'; opossum: 5'-TCACCGCTCTCAACCTCGTT-3' and 5'-TAGGAATTGGTCAAGAGACTTCCA-3'). Mouse E10 and E11 samples were pooled from 2-4 littermates: the first E10 pool contained 3 female cerebella and the second 2 female and 2 male cerebella; the first E11 pool contained 2 male cerebella and the second 2 female cerebella (table S1).

Single nucleus ATAC-seq data generation

To isolate nuclei from frozen pre- and postnatal cerebellum samples we used a published protocol (*52*), which we optimized with the aim to maximize the recovery of nuclei. The frozen tissue was homogenized on ice in 250 mM sucrose, 25 mM KCl, 5 mM $MgCl_2$, 10 mM Tris-HCl (pH 8), 0.1% IGEPAL, 1 µM DTT, 0.4 U/µl Murine RNase Inhibitor (New England BioLabs), 0.2 U/µl SUPERas-In (Ambion), cOmplete Protease Inhibitor Coctail (Roche) by trituration and/or by using a micropestle. After 5 minutes incubation the remaining bits of unlysed tissue were pelleted by centrifugation at 100 g for 1 minute. The cleared homogenate was centrifuged at 400 g for 4 minutes to pellet the nuclei. Nuclei were washed in the homogenization buffer 1-2 times (table S1), collected by centrifugation and resuspended in the Nuclei Buffer (10x Genomics). If needed the nuclei were strained using 40 µm Flowmi strainers (Sigma) to remove nuclei aggregates. For estimation of nuclei concentration, Hoechst DNA dye was added and

nuclei were counted on Countess II FL Automated Cell Counter (Thermo Fisher Scientific; RRID:SCR_020236). 15,000 nuclei per sample were subjected to tagmentation, single cell barcoding and library construction using the Chromium Single Cell ATAC Reagent kits (v1 for mouse and v1.1 for opossum data production) and Chromium Controller instrument (10x Genomics; RRID:SCR_019326) according to the manufacturer's protocols. Libraries were amplified in 10 PCR cycles and quantified on Qubit Fluorometer (Thermo Fisher Scientific; RRID:SCR_018095). Average fragment size was determined on Fragment Analyzer (Agilent; RRID: :SCR_019417). Libraries were sequenced on NextSeq 550 (Illumina; RRID:SCR_016381; 34 cycles for both Read 1 and Read 2, 8 cycles for i7 index and 16 cycles for i5 index) with an average of 229 million read pairs per library.

Mouse snATAC-seq processing and quality control

Raw sequencing data were demultiplexed and converted to fastq format using cellranger-atac mkfastq (1.1.0) (*21*). The command cellranger-atac count (1.1.0) was used to correct droplet barcodes for sequencing errors, align reads to the mouse genome (mm10), generate position-corrected tabular fragment files and identify PCR duplicates from fragments with identical positions originating from the same droplet barcode. Position-corrected fragments were used as an input to ArchR (0.9) for subsequent processing, quality control and analysis (*22*). Using ArchR's precompiled genome and gene annotations for mm10 we tiled the genome in 500 bp bins, counted fragments per barcode and bin, and inferred gene scores as a proxy for gene expression. Briefly, ArchR estimates gene scores by counting all fragments overlapping a gene's body and a region 5,000 bp upstream of the transcription start site (TSS). Additionally, it incorporates information from distal regulatory elements within a 100 kb window, as long as there is no TSS from another gene in between. Information from distal CREs is weighed by distance using an exponential decay function ($e^{(-abs(distance)/5000)} + e^{-1}$). Thus, CREs closer to the gene contribute more to its activity estimate. Additionally, the estimate is adjusted for gene length by multiplying with [5/gene size]. Finally, estimates are normalized for sequencing depth to a total of 10,000 per cell. The model used

was found to perform best in the prediction of gene expression estimates from snATAC-seq data based on comparisons with matched scRNA-seq data (*22*).

Quality control at the library level was performed by observing the expected periodicity in the frequency of fragment sizes (fig. S2A) and enrichment of insertions around annotated TSS (fig. S2B). Additionally, following the identification of putative CREs active in cerebellum development (see below) we aggregated accessibility profiles for autosomal CREs across all cells in each sample (i.e., snATAC-seq library) and estimated rank based Spearman's correlations across the accessibility profiles across samples (fig. S2F).

Cell identification and doublet removal

Barcodes corresponding to nuclei of cells were distinguished from empty droplets by requiring at least 5,000 fragments and a minimum TSS enrichment of 3. A total of 117,713 barcodes passed this first filtering step. A common issue of single-cell technologies arises from two or more cells being included in the same droplet and thus sharing the same barcode. Such putative doublets were identified *in silico* using the function addDoubletScores() from ArchR. This method is based on simulating artificial doublets by adding up the fragment counts of random cell pairs from the same sample. The simulated doublets are co-embedded with the real cells and putative doublets are identified as cells that are consistently found near simulated doublets in the embedding. We used latent semantic indexing (LSI, as described in *"Dimensionality reduction and clustering"*) to embed our cells into 50 dimensions and performed 10 trials, each marking the 10 nearest neighbors of every simulated doublet. Cells from the same sample were then ranked based on their doublet enrichment score, i.e., the number of simulated doublets identified as a nearest neighbor divided by the expected number given a random uniform distribution. We then used the function filterDoublets() to remove the top X% of cells from each sample, where X is proportional to the number of cells per sample, as the fraction of expected doublets depends linearly on the number of loaded cells (*21*). We used a filterRatio of 1, removing 5% from a sample of 5,000 cells (1st

pass doublets). 111,201 cells passed this filtering step. However, in downstream stages of the analysis we noticed that cells with high number of fragments and doublet enrichment scores were clustering together. We thus implemented an additional filtering step, removing all cells with more than 45,000 fragments (approximately double the median number of fragments per cell) or a doublet enrichment score greater than 4 (fig. S2C). This filtering step removed an additional 13,855 cells (2^{nd} pass doublets). We also marked six clusters that were enriched for these putative doublets (fig. S2D). To assess whether the remaining cells in these clusters also corresponded to doublets or low quality cells, we identified marker genes per cluster using the gene score matrix as an input to the function getMarkerFeatures() from ArchR. Even after removing the 1^{st} and 2^{nd} pass doublets, four of the six clusters (C5, C18, C21, C55) showed no enrichment for gene activity or a mixture of marker genes for distinct cell types present in the same sample. Thus, we decided to exclude all cells belonging to these four spurious clusters from subsequent analyses. This iterative, stringent filtering procedure resulted in a total of 91,922 cells with a median of 20,558 unique fragments per cell and a median TSS enrichment score of 7.8. Following cell type annotation (see *"Iterative clustering and cell annotation")* a total of 2,435 cells could not be confidently assigned to a cell type and were labeled as "Low quality". Although lower than the cutoffs used for doublet detection, these cells have significantly higher doublet enrichment scores (median: 0.96 versus 0.21 for all other cells, $P < 10^{-15}$, Mann-Whitney U test) and showed no enrichment for marker genes or differentially accessible CREs (fig. S10A), suggesting that they might correspond to doublets or mixtures of low quality cells that cannot be distinguished from each other. We thus excluded these cells from all analyses downstream of dimensionality reduction, clustering and peak calling.

Dimensionality reduction and clustering

We used ArchR's iterative implementation of latent semantic indexing (LSI), which assigns higher weight to cell type-restricted CREs, while filtering out features that show low-level, noisy activity across cells in a cell type-independent manner. We used five iterations, each time sampling 20,000 cells (10,000 for subclustering analyses, see *"Iterative clustering and cell type annotation"*) with ten random starts and

gradually increasing the clustering resolution (0.1, 0.2, 0.4, 0.8). We used 500 bp-wide genome tiles as input to avoid biases against rare cell types and states, excluded mitochondrial and sex chromosomes and binarized the count matrix. Features were transformed with TF-log(IDF) and the 100,000 most variable features (50,000 for subclustering analyses) were reduced to 100 dimensions with singular value decomposition (SVD; 50 dimensions used for subclustering analyses). Each component was weighed by the percentage of variance it explained. Components showing an unusually high correlation with sequencing depth (Pearson's $r > 0.75$) were excluded from downstream analyses. These SVD components were used as input for Louvain clustering and projection to a UMAP embedding.

Iterative clustering and cell type annotation

The multidimensional nature of our dataset poises challenges to cell type annotation as similarity between cells might be driven by factors other than cell type identity, such as developmental stage, or differentiation and maturation state. To overcome this challenge, we implemented an iterative clustering approach to identify high quality cells and assign them to cerebellar cell types and states. First we applied Louvain clustering to the full dataset, identifying 47 distinct clusters (resolution 1.5; fig. S2E, S3A). We used gene score as a proxy for gene expression to assign clusters to putative cell types and states based on previously described marker genes (*2*, *24*), as well as manual investigation of *in situ* hybridization data from the Allen Developing Mouse Brain Atlas resource (*49*). We observed that many of our clusters contained additional substructure, which we were unable to recover when considering the entire dataset, even when increasing the clustering resolution. Thus, we decided to subcluster cells from clusters where additional structure was apparent (fig. S3B-D). We grouped these cells into three broad groups (astroglia, early-born neurons, and GABAergic neurons from E13) and repeated the LSI dimensionality reduction and clustering (38, 37 and 21 subclusters obtained with a resolution of 2.5, 2.5 and 2.0 respectively). We followed the same approach, relying on gene score of marker genes to identify cell types and their subtypes. Cluster 3 from the astroglia group was further split into three subclusters. We then assigned each cell to the most specific cell type and state label available from the full dataset or subclustering

analysis. In the astroglia group we identified 222 contaminating brainstem progenitor cells (80% of which from E10-E12, fig. S3B), characterized by high gene score for several Hox genes (*Hoxc13, Hoxc6, Hoxc4, Hoxa3*), which are expressed in the lower brainstem (pons and medulla) but not in the cerebellum (*3*). Following inspection of individual developmental stages, we identified a total of 2,435 cells (E11: C13, E12: C14-C15, P14: C12) that could not be confidently assigned to a specific cell type and that likely include remaining doublets or unresolved clusters (see *"Cell identification and doublet removal"*), which were labeled as "Low quality" cells. Taken together, we were able to provide broad cell type and subtype/cell state labels to 97% of the cells in the mouse dataset.

Integration with mouse cerebellum scRNA-seq data

We used single-cell RNA-seq data from a previous study which profiled mouse hindbrain and cerebellum development (*23*) to compare cell type annotations and assess the utility of gene scores as a proxy for gene expression. To improve the computational efficiency and accuracy of our approach we performed the integration in a stage-wise manner, matching developmental stages between studies as closely as possible. We obtained gene by barcode matrices of UMI counts (GEO accession number: GSE118068) and reprocessed the data separately for each stage using a standard Seurat pipeline (3.0.1) (*53*). Briefly, we only used high quality cells, as previously filtered by the authors, applied SCTransform() to scale the data and identify highly variable genes, and reduced the dimensions of the data to 50 principal components.

We reprocessed our snATAC-seq data separately for each developmental stage as described above (see *"Dimensionality reduction and clustering"*; fig. S5) with the following modifications: 50,000 variable features, 50 SVD components, clustering resolution of 1.0. When analyzing the data in a stage-wise manner, we observed small separation between replicates in the P14 and P63 datasets. Given the very high correlation between the biological replicates (Spearman's rho: 0.98 for both stages), we reasoned that the separation between replicates was more obvious due to the low cellular complexity of these

samples, which are both dominated by granule cells. We corrected these mild batch effects using Harmony (1.0) in the LSI space (*50*). Although batch effects were only visible in P14 and P63, we applied the Harmony correction to all stages for consistency in our analysis. We then created a custom Seurat object containing the gene scores, metadata and embeddings of each snATAC-seq sample.

The integration between matching snATAC-seq and scRNA-seq datasets was performed separately for each developmental stage using canonical correlation analysis (CCA) as implemented in Seurat (*53*). We used the following ATAC-RNA matches: E10-E10 (cerebellum-hindbrain), E12-E12 (cerebellum-hindbrain), E13-E14, E15-E16, E17-E18, P0-P0, P4-P5, P7-P7, P14-P14. E11 and P63 were not considered for this analysis as no matching scRNA-seq data were available. Additionally, the scRNA-seq datasets for P5 and P14 did not contain cell type annotations and were thus only used for imputing gene expression. scRNA-seq UMI counts and snATAC-seq derived gene scores were scaled down to 10,000 counts per cell. We used the intersect between highly variable genes from the scRNA-seq sample and genes for which gene score estimates were available in the snATAC-seq sample as features to identify transfer anchors in the CCA space, using the command FindTransferAnchors() with the scRNA-seq object as reference and the snATAC-seq object as query. We then applied the command TransferData() to transfer cell type labels (when available) and scRNA-seq UMI counts to the snATAC-seq Seurat object using the 10 (for cell type labels) or 15 (for RNA imputation) nearest neighbors in the LSI space to weigh the predictions.

We next used the cell type labels predicted from the integration to compare to our cell type annotations. Each cell in our snATAC-seq dataset (for stages E10, E12, E13, E15, E17, P0 and P7) had a cell type label assigned by our iterative clustering approach and a predicted label transferred from the integration with the scRNA-seq data. We estimated a Jaccard similarity index for each pair of ATAC and RNA labels by dividing the number of cells with both labels over the number of cells having either of the two labels. This allowed us to identify pairs of labels used by the two studies to describe similar cells and manually

curate whether these labels describe the same or similar cell type populations. This approach allowed us to examine one-to-many and many-to-many matches, which occur often because the two studies annotate cells at different resolutions (for example we identified more subtypes for progenitors and early-born neurons whereas the RNA-seq study identified more non-neural cell types). Additionally, the developmental nature of our datasets produces many-to-many matches between differentiation states with arbitrary boundaries (e.g., differentiating and mature neurons). Overall, we observed high confidence in cell type predictions (median prediction score: 0.81) and a good concordance between the two annotations (fig. S6B-C). We manually examined discrepancies in cell type predictions by investigating the scRNA-seq clusters annotated as "excitatory" (glutamatergic) (deep) "nuclei neurons" and UBCs, identifying additional substructure, which suggests that these scRNA-seq clusters correspond to mixtures of different cell types (fig. S6D-E).

To assess the utility of gene scores for predicting gene expression in our data we focused on the genes used for the integration (highly variable genes in the scRNA-seq data with gene score estimates in the snATAC-seq data) and averaged expression estimates across clusters in the snATAC-seq data. We then calculated Pearson's correlations per gene between the gene score and imputed RNA expression across clusters. We observed robust correlations between the two estimates (median across all genes and stages Pearson's *r*: 0.5; fig. S6A), motivating us to use gene scores as a proxy for gene expression for downstream analyses. We preferred gene scores to imputed RNA expression because 1) we had estimates for all cells (E11 and P63 had no matched scRNA-seq data) and 2) it was derived directly from our data, thus overcoming issues with the compatibility of the dissections and developmental stages between the two studies. Additionally, for specific claims regarding the effect of chromatin accessibility changes on gene expression, we examined the raw scRNA-seq data (e.g., fig. S12E-F and fig. S16H).

For the co-embedding of snATAC-seq and scRNA-seq data presented in fig. S6C, we used real (for scRNA-seq cells) and imputed (for snATAC-seq cells) expression values for the highly variable genes in

the scRNA-seq dataset to project cells into 25 principal components as implemented in Seurat (*53*). These components were further corrected across samples using Harmony (*50*) and provided as input for UMAP dimensionality reduction in Seurat (15 nearest neighbors, cosine distance, minimum distance=0.15). To facilitate comparisons between cell type annotations between studies (also as in fig. S6F), cell labels were collapsed into broad groups of cell types ('Astroglia' includes all proliferating progenitor, stem cell and astrocyte categories; 'Early neurons' comprise parabrachial, deep nuclei and nuclear transitory zone populations; 'GC/UBC' groups granule cells and unipolar brush cells; Purkinje cells, interneurons, microglia and oligodendrocytes are kept as separate categories; all other cell types are marked as 'Other'). We note that this co-embedding only serves visualization purposes.

Identification and annotation of putative CREs

Cluster and sample-based pseudobulk generation and peak calling

We used ArchR's function addReproduciblePeakSet() to identify regions of accessible chromatin, as a proxy for putative CREs (fig. S7A). We opted for this framework because it allowed us to account for differences in the abundance and heterogeneity of cell types in our dataset and to utilize our biological replicates to assess peak reproducibility. Briefly, we used the 47 clusters from the full dataset to generate pseudobulks comprised of cells from the same cluster and sample (biological replicate). This allowed us to identify cell type/state-specific peaks while retaining the information of the sample the cells came from (and thus filtering out irreproducible peaks). Depending on the number of cells contained in each sample, we constructed 2-10 pseudobulk groups, each containing a minimum of 100 and a maximum of 1,000 cells, while limiting the maximum number of fragments per sample to 50 million. The minimum threshold for the number of cells per group (100) was estimated by subsampling analysis as the minimum number required to obtain a Pearson's correlation of at least r=0.95 with the entire pseudobulk of a given cluster. The rationale behind setting a maximum threshold was to limit the contribution of very abundant cell types and states (e.g., mature granule cells) to the peak set. We chose to restrict this parameter through the number of cells in a group (1,000) rather than the number of samples, to facilitate the

identification of CREs from cell types that are consistently rare in our data but present in multiple samples (e.g., microglia or postnatal Purkinje cells). If a cluster did not have 100 cells from at least two samples, we allowed up to 80% of the cells from a group to be resampled with replacement to reach the required number. In practice, this only affected two clusters (C1: erythroid and C15: mature UBCs). We then called peaks within each group (cluster + sample) using MACS2 (2.1.2) (*54*) through ArchR with the following parameters "--shift -75 --extsize 150 --nomodel --call-summits --nolambda --keep-dup all -q 0.01" and excluding chromosome Y. We allowed up to 200,000 peaks to be identified from a single group, or up to 1,000 peaks per cell (thus for a group of 50 cells that would be 50,000 peaks).

Union peak set generation

Calling peaks in a cluster- and sample-aware manner resulted in multiple peak sets that had to be collapsed into a single peak annotation. Given that many of our subsequent analyses depended on the overlap with various genomic elements (see *Peak annotation*), which can be biased by the width of each peak, we followed ArchR's iterative overlap merging procedure to obtain the maximum number of 500 bp-wide non-overlapping peaks (fig. S7A). Briefly, ArchR's approach is based on extending peak summits from each group by 250 bp in each flank, then identifying overlapping windows and ranking them based on peak's significance, normalized by the sequencing depth of each group. The most significant peak is retained and all other overlapping peaks are removed. This approach avoids chain-merging of adjacent peaks as well as the removal of peaks that are proximal but non-overlapping to the most significant peak (*22*). We required each peak to be supported by at least two biological samples (i.e., replicates), which resulted in 499,146 non-redundant peaks (permissive peak set). To avoid the inclusion of noisy peaks from clusters with very large numbers of cells or replicates, we further filtered for peaks that were active in at least 5% of at least one cluster (robust peak set; fig. S7A-B). These robust peaks were associated with higher summit scores and reproducibility and were enriched for overlap with H3K27ac histone marks during hindbrain development. Thus, reasoning that these robust peaks were more likely to correspond to putative CREs, we limited all our downstream analyses to this set. However,

we also provide the permissive set as a resource as it could contain CREs with more restrained activity to specific cell types/states (https://apps.kaessmannlab.org/mouse_cereb_atac/).

Peak annotation

ArchR automatically annotated peaks based on their genomic context as promoters (-2,000/+100 bp from a TSS), exonic, intronic or intergenic based on UCSC annotations for the mm10 genome (*55*). We integrated this annotation with the biotypes of the associated gene, acquired from Ensembl Biomart (v94) (*56*), and collapsed to four main biotypes: protein-coding, lncRNA (including antisense, bidirectional and intergenic lncRNAs), small RNA (miRNA, snRNA and snoRNA) and other (mostly pseudogenes). We further supplemented the UCSC annotation with a previously described set of lncRNAs expressed during mouse organ development (*40*). We used bedtools intersect (2.29) (*57*) to identify overlaps between peaks and lncRNA promoters, exons and gene models, updating the annotations of previously intergenic and intronic CREs based on their overlap with lncRNA features.

To determine peak overlap with TF motifs and to assess TF activity based on the aggregate accessibility of these motifs, we used the ArchR implementation of the package chromVAR (*58*). We scanned our peak set for instances of the motifs present in the cisBP collection (*59*) using the default cutoff of $P < 5e-05$. We then computed per-cell deviations for all motifs using a GC-content matched background peak set.

To assess sequence constraint in putative CREs we used estimates of evolutionary conservation (phastCons scores) based on multiple alignments (*41*). We downloaded phastCons scores for vertebrates and eutherian mammals (commonly referred to as placental mammals) for mm10 as bigWig files from the UCSC table browser. As selective constraint is often concentrated to specific regions of a CRE (e.g., TF binding sites), we employed a sliding window approach to identify the most conserved 100 bp region of

each CRE using the UCSC utility bigWigAverageOverBed (*60*). The mean phastCons score within the most conserved 100 bp region was considered as a metric of constraint for each CRE.

To assign a minimum evolutionary age for each putative CRE we assessed the presence or absence of the putative CREs in the genomes of other species based on syntenic alignments between mouse and 16 high quality vertebrate genomes of various phylogenetic distances (fig. S15A and table S6). We downloaded chain alignments from UCSC and used liftover (-minMatch=0.1 -multiple -minSizeQ=50 -minSizeT=50) to identify syntenic regions in each species. We then assigned a putative age to each CRE based on the estimated age of divergence between mouse and the most distant species in which a syntenic region could be detected (from *timetree.org*). We observed that older regions were also found in more species, suggesting that the number of false positive alignments was overall low (fig. S15B).

To determine the contribution of transposable elements to the identified putative CREs, we used bedtools (2.29) (*57*) to intersect our CREs with the RepeatMasker track for the mm10 genome, downloaded from UCSC Table Browser (*61*). Per CRE, we estimated the fraction covered by repeats and retained the name and class of the overlapping repeats.

Benchmarking of putative cerebellum CREs with external datasets

We compared the identified putative CREs with relevant bulk and single-cell datasets from previous studies. We downloaded Encode chromHMM annotations (*11*) for mouse candidate CREs for different tissues and developmental stages (table S6) and intersected them with our peaks using bedtools (2.29) (*57*). For each sample (tissue and developmental stage) we estimated the fraction of Encode-annotated enhancers ("Enh") and heterochromatin ("Het") elements that overlapped our peaks. Additionally we examined the overlap of CREs with experimentally validated hindbrain enhancers (*28*) (fig. S7E). For representative examples, we compared the activity specificity (as assessed from *LacZ* reporter stainings) to the accessibility profiles of overlapping CREs (fig. S7F). We also compared to a dataset of transcribed

enhancers (eRNAs) across a wide range of mouse samples (*29*). We obtained binary activity matrices for eRNAs across samples, intersected eRNA coordinates with the CREs identified in our study and estimated the fraction of eRNAs active in each sample that is captured in our CRE set. We then compared these fractions between samples from the cerebellum, other neural tissues, whole embryo development, and all other sources (fig. S7G). Finally, we also benchmarked our peak set against a published single-cell atlas of chromatin accessibility in adult mouse organs (*15*). After identifying overlapping peaks using bedtools intersect, we estimated the fraction of reads per cell in the mouse atlas within regions overlapping our peak set (fig. S7H).

Assignment to putative target genes

As CREs can act over larger distances in the linear genome, the identification of their target genes is particularly challenging. Whereas *bona fide* regulatory interactions can only be established by perturbation or genetic studies, CREs and their target genes are expected to be active in the same cell types/states. We thus used a correlation-based approach across cell types and states in our dataset to assign distal (intronic and intergenic) CREs to their putative target genes, akin to previous studies (*11*, *16*). To increase the confidence of our assignment, we used a combination of two different features, as well as estimates of correlations across different parts of the dataset (fig. S8A).

First, we estimated the co-accessibility of protein-coding gene promoters and distal CREs within a 250 kb window upstream and downstream from the promoter. To account for the sparsity of single-cell data, we used ArchR to create 5,000 pseudocells (groups of 50 nearest neighbors based on their distance in the LSI space) and aggregated their accessibility profiles. Pseudocells showing more than 50% overlap in their members with another aggregate were excluded resulting in a total of 4,083 groupings. The aggregated accessibility profiles were scaled by sequencing depth, log transformed and used to compute pair-wise Pearson's correlations between promoters and distal CREs. To assess the significance of these correlations we generated a background distribution by sampling for each promoter 10,000 random distal

CREs from different chromosomes and estimating correlations. We used the R package fitdistrplus (1.0) (*62*) to convert these correlations into a null distribution. We then used this null distribution to estimate probabilities for the observed correlations between promoters and CREs in the 250 kb window, which we adjusted for multiple testing using the Benjamini–Hochberg (BH) procedure. Since promoter accessibility often poorly correlates with gene expression (*22*), we used a lenient cutoff of $r > 0.15$ (FDR < 40%) as a first filtering step.

As a second step, we focused on gene scores, which reflect gene expression more accurately than promoter accessibility (*22*). We opted for using gene scores over imputed gene expression from the integration with the scRNA-seq data (see *"Integration with scRNA-seq data"*), because matched transcriptomics data were not available for some stages due to differences in dissections and sampling, whereas the two metrics were overall highly correlated in properly matched stages (fig. S6A). We focused on gene-distal CRE pairs that passed the first filtering step based on promoter co-accessibility (considering the promoter with the highest correlation for genes with multiple promoter CREs). A limitation of gene scores is that information from distal CREs is already incorporated in the estimate, which can lead to spuriously high correlations at the level of cells or pseudocells due to shared confounders, such as small deviations in the accessibility of distal CREs across cells, even when variance across cell types and stages is low. To focus on the latter, which is more likely to reflect biologically relevant interactions, we aggregated gene score and distal CRE accessibility estimates at the level of pseudobulks, comprised of all cells from the same cell type/state (as in Fig. 1C, excluding vascular, erythroid, apoptotic GCs and low-quality cells) and developmental stage. We considered groups of at least 40 cells, summed gene score and accessibility estimates, scaled by sequencing depth and log transformed before computing Pearson's correlations across a set of 124 pseudobulks. We generated a background distribution using interchromosomal correlations as described for the promoters and assessed probabilities for the observed correlations adjusting for multiple testing (Benjamini–Hochberg

procedure). For this second step we used a strict cutoff of $r > 0.41$ (FDR < 5%). Finally, we assigned distal CREs correlated to multiple genes to the gene with the highest correlation.

This two-step approach allowed us to consider estimates of both promoter accessibility and gene score activity. In the first step, where promoter and distal CRE accessibility measurements are independent from each other, we used the full power of our dataset to compute correlations across a large number of pseudocells, which incorporate both biological and technical variation. In the second step, we collapsed estimates across cell states and developmental stages, reducing the contribution of technical factors such as fluctuations in accessibility and differences in abundances between cell types. However, an inevitable limitation of our approach is that we can only identify CRE-gene interactions for elements with dynamic activity across cell types and stages.

To assess the confidence of our CRE-gene assignment, we compared with previously published datasets. First, we examined topologically associating domain (TAD) annotations from *in vitro* cultured neural progenitors (*30*), since regulatory interactions occur more frequently in the same TAD. We intersected all distal CREs and promoters that we tested for this analysis with TAD coordinates from the published study and compared how often they were in the same or different TADs across significant and non-significant interactions (fig. S8B). The single-call category refers to cases where only one CRE (distal or promoter) overlaps a TAD. Second, we examined a dataset of enhancer RNAs (eRNAs) and promoter-associated transcripts, profiled using Cap Analysis of Gene Expression (CAGE) in a series of samples from embryonic and postnatal cerebellum (*29*). We obtained raw count data and scaled them as transcripts per million (TPM) using the RLE normalization from the package edgeR (3.28) (*63*). We then estimated Pearson's correlations across cerebellum samples between pairs of eRNAs overlapping our distal CREs and CAGE peaks overlapping our promoters and compared the distribution of correlation coefficients between significant and non-significant interactions. Finally, we used Fisher's exact tests to estimate

enrichments of distal CREs overlapping enhancers active in the hindbrain according to chromHMM models (*11*) and experimental validation in E11 embryos (*28*) in significant interactions.

CRE activity across cell types and developmental stages

To profile the activity of CREs during the development of different cerebellar cell types (Fig. 2B), we aggregated the activity of all cells into pseudobulks for a given cell type and developmental stage. We excluded samples from cell type mixtures (e.g., nuclear transitory zone, parabrachial and isthmic nuclei, low-quality cells) and non-neural cell types (e.g., erythroid, vascular). We only used pseudobulks comprised of at least 50 cells, which we determined as the minimum number of cells required to obtain a Pearson's *r* correlation coefficient of at least 0.9 compared to the full pseudobulk in a subsampling analysis of P63 granule cells (fig. S9A). Only robust CREs were considered for this analysis. We scaled the data in counts per million (CPM) to account for differences in cell numbers and sequencing depth. We then standardized estimates per CRE by scaling by its maximum CPM value across all groups.

We used a two-stage clustering approach inspired by a previous study (*64*). First we performed K-means clustering with a high number of primary clusters (n=50). Then, for each primary cluster we estimated the mean activity pattern and used it as input for hierarchical clustering (based on the correlation distance matrix between cluster centers). We then used the clustering dendrogram to iteratively merge the two most similar branches and compute the silhouette score for each new set of clusters. We determined the optimal number of final clusters to be 26, based on the distances between the hierarchical clustering branches, the silhouette score distribution of each iterative merge, and the original number of optimal clusters suggested by the silhouettes of different K-means runs.

We further assessed the clustering quality for each CRE by estimating the correlation between its activity and its cluster's mean. The median Pearson's *r* estimate for a CRE with its own cluster was 0.63. CREs with a correlation estimate of at least 0.5 with their cluster center were considered to be "confident cluster

members" (fig. S9B). These "confident cluster members" were associated with gene ontology terms based on their nearby genes using GREAT and enriched TF motifs using Homer (see *Characterization of enriched peak sets*). To visualize the clustering results (fig. 2B), we randomly selected 50,000 CREs (with $r > 0.5$ to their cluster mean or belonging to the ubiquitously active cluster) and plotted their standardized activity across cell types and developmental stages in a heatmap. We chose random selection over prioritizing highly variable features to better represent the true proportions of CREs in each cluster.

To generate custom tracks of cell type- and time-specific CRE activity for the UCSC genome browser (http://genome.ucsc.edu/s/ioansarr/Mouse%20cerebellum%20snATAC-seq%20cCREs), we used the same pseudobulks generated for the clustering analysis. We selected active CREs per cell type and developmental stage as those with CPM ≥ 5 and exported them in bed format. Bed files per cell type and stage were subsequently uploaded to the UCSC browser.

To identify differentially accessible CREs, we used the function getMarkerFeatures() from ArchR, grouping the cells by cell type and state (as in Fig. 1C). Marker CREs were identified based on "Wilcoxon" tests at an FDR < 0.01 and with a $\log_2$ fold-change of at least 3.0. We additionally subset the markers for robust CREs (accessible in at least 5% of the cells in at least one cluster) and only considered CREs that are markers for a single group. For the identification of differentially accessible CREs between pre- and postnatal granule cell progenitors, we aggregated the accessibility profiles of cells within each sample (developmental stage and replicate), only considering groups of at least 100 cells. We then used DESeq2 (1.26) (*65*) to identify differentially accessible CREs between pre- and postnatal samples requiring a Benjamini-Hochberg adjusted *P*-value < 0.05 (with an alpha of 0.5) and an absolute $\log_2$ fold change >1.5.

Characterization of enriched CRE sets

Throughout this study we aimed to characterize groups of CREs with similar activity patterns (e.g., belonging to the same cluster, showing differential accessibility across developmental stages or during differentiation). To associate CREs with the biological processes (BP) of their putative target genes we used the R implementation of GREAT (rGREAT, 1.18.0) (*66*) to identify enriched gene ontologies. We preferred considering adjacent genes over our correlation-based gene assignment, as the latter only assigned a limited number of CREs to target genes with high confidence. Similarly, we used Homer (4.11.1) (*67*) to identify enriched TF motifs in each cluster of CREs. We performed motif search using the command findMotifsGenome.pl with the options –gc to account for GC content biases and –size given to scan the entire peak regions. For both BP and motif enrichment all CREs tested in the analysis were combined and used as a background peak set. The *P*-values of the enrichment of each term for each CRE set were capped for visualization purposes (typically to 10^{-100} for motifs and 10^{-30} for BP enrichment) and plotted in a heatmap. For BP enrichment, when the number of CRE sets was large and/or processes were too similar, we collapsed BP terms to a non-redundant set using Revigo (*68*) with the following parameters: allowed similarity: 0.5, semantic similarity measure: SimRel.

Annotation and clustering of cerebellar progenitors

The identification of progenitor types was performed using the iterative clustering procedure in the entire dataset as discussed in *"Iterative clustering and cell type annotation"*. Contaminating brainstem progenitors were excluded from this analysis. Marker genes per progenitor type and developmental stage were identified using the function getMarkerFeatures() from ArchR, filtering for FDR < 0.01 and $\log_2$ fold-change > 1. For plotting, marker genes were prioritized based on the product of their $\log_2$ fold-change estimate and the $-\log_{10}$ *P*-value of the test. For the UMAP embedding presented in Fig. 3, we applied the IDF transformation to robust CREs accessible in at least 1% of the cells and projected them into 50 components using SVD. We chose a single-step IDF-SVD analysis over an iterative LSI (see *"Dimensionality reduction and clustering"*), to ensure that the separation between developmental stages

was not due to the amplification of signal from CREs with variable accessibility across clusters. We excluded the first component, which showed high correlation with sequencing depth, and used the remaining components for UMAP dimensionality reduction.

We aggregated chromatin accessibility across cells from the same progenitor type and developmental stage and scaled to a total of 10^6 fragments per group. Only pseudobulks with at least 100 cells and robust CREs that reached at least 5 CPM in at least one pseudobulk (122,572 putative CREs) were considered for subsequent analyses. For the clustering across progenitor types and stages, we calculated Spearman's correlation coefficients across the pseudobulk samples (i.e., progenitor type and stage) and performed hierarchical clustering using ward.D2 and pairwise complete observations. To assess the robustness of the clustering we used bootstrapping as implemented in the package pvclust (*69*) with 1,000 repetitions. To identify patterns of CRE activity in progenitor cells we standardized the 122,572 putative CREs by their maximum activity across the progenitor samples and then used the clustering approach described in *"CRE activity across cell types and developmental stages"*. For this analysis we generated 30 clusters with k-means clustering, which we then collapsed to a final number of 12 clusters based on hierarchical clustering of their cluster means.

For the analysis focusing on the similarity between white matter and granule cell layer astroblasts to earlier progenitor populations (bipotent, gliogenic), we used ArchR's getMarkerFeatures() to identify CREs that are specific to each astroblast population, filtering for FDR < 0.01 and $\log_2$ fold-change > 1. We then estimated the fraction of fragments per cell from earlier progenitor populations (bipotent, gliogenic in E17, P0) that overlap CREs specific to each astroblast population. We used the same approach to assess the relationship between anterior ventricular zone and bipotent progenitors. We first extracted progenitors from the developmental stages E13-E15 and identified CREs that are specific to each germinal zone, as described above. This led to the identification of 1,753 CREs, 238 of which showed significantly higher accessibility in bipotent progenitors. We then estimated the fraction of

fragments per cell that overlap those CREs and compared early (E10-E12) progenitor populations of different germinal zones. As a complementary analysis, we aggregated accessibility profiles across cells from the same progenitor type and developmental stage and estimated Spearman's correlations between bipotent progenitors from E13 and E15, and early (E10-E12) progenitor populations based on the 122,572 putative CREs considered for the progenitor analysis.

Identification of temporally-variant genes in progenitors

We used a variance-based approach to identify genes with coordinated temporal changes across progenitor types. We aggregated cells from the same progenitor type, developmental stage and replicate, only considering groups with at least 50 cells, and estimated mean values for gene score activities. Given that some progenitor types are limited to specific developmental stages we then split our dataset into two groups: early progenitors (E10-E13; uncommitted, isthmic, anterior ventricular zone, ventricular zone, rhombic lip) and late progenitors (E15-P0; bipotent and gliogenic). Within each group, we identified the 2,000 genes with the highest variance (using the aggregated profiles across progenitor types, stages and replicates). Focusing on these genes, we grouped samples from the same progenitor type across all stages, estimated gene score averages and computed the standard deviation of each gene across progenitor types (progenitor type SD). Similarly, we grouped by developmental stage, averaged across all progenitor types and computed the standard deviation of each gene across developmental stages (developmental stage SD). Additionally, we estimated standard deviations between replicates for groups from the same progenitor type and developmental stage, and averaged these estimates to compute a single metric of standard deviation across replicates per gene (replicate SD). We then calculated the ratios of the standard deviations [developmental stage SD/cell type SD] and [developmental stage SD/replicate SD]. Temporally-variant genes were identified as those with a $\log_2$ fold-change > 1.25 in both comparisons. We then clustered these temporally-variant genes with a fuzzy c-means clustering algorithm for time series from the R package Mfuzz (2.46.0) (*70*) using k=2 to identify genes with increasing and decreasing gene score activity during development. To assess whether the observed differences in chromatin

accessibility lead to changes in gene expression we examined the aggregate expression of temporally variant genes with increasing and decreasing gene score activity in the published scRNA-seq data (*23*). Specifically, for each progenitor cell in the RNA-seq dataset (as annotated by the authors) we estimated the fraction of UMIs in each gene set (increasing/decreasing gene score activity). We then grouped cells by developmental stage and compared the aggregate expression of each gene set during development. We note that due to differences in the number of genes in each set (as well as technical biases in the detection of genes with different intron lengths in 10x Chromium 3' scRNA-seq data) comparisons are only meaningful across developmental stages for the same gene set but not between gene sets. Finally, we also compared the distribution of $\log_2$[developmental stage SD/cell type SD] for the 2,000 most variant genes in the early and late progenitor populations as a metric of temporal versus spatial variance in different stages of development.

Cell type differentiation

For each of the three most abundant cerebellar neuron types (granule cells, Purkinje cells and interneurons), we identified cells assigned to that cell type and analyzed them separately. We only considered developmental stages with at least 100 cells assigned to the specified cell type. We applied the IDF transformation to robust CREs accessible in at least 1% of the cells and embedded the data into 20 components using SVD. In agreement with previous studies (*15*), the first SVD component showed very high correlation with the sequencing depth of each cell and was therefore excluded from downstream analyses. We chose a single-step IDF-SVD analysis over an iterative LSI (see *"Dimensionality reduction and clustering"*), because the latter, although useful for the identification of distinct cell types in the full dataset, exaggerates differences between cells by prioritizing CREs with variable accessibility across clusters (the borders of which are arbitrary in developmental or spatial gradients). We also observed that performing the IDF transformation without scaling by each cell's sequencing depth (TF) and omitting the 1st SVD outperformed the standard TF-IDF in capturing continuous differentiation signals (inferred based on the activity of known marker genes).

As we observed developmental signal that was orthogonal to differentiation (e.g., pre- and postnatal granule cell progenitors and differentiating cells), these components were further corrected using Harmony (1.0), a single-cell integration algorithm that relies on soft-clustering, thus allowing for smooth transitions between cell states, such as those observed during cell differentiation (*50*) (fig. S13A-C). To allow for differentiation states unique to individual developmental stages (e.g., differentiating Purkinje cells in E12) we set the ridge regression penalty parameter to a relatively large value (lambda=5). The obtained Harmony-corrected dimensions were then used as input for clustering and UMAP projection.

We used diffusion-based pseudotime (*51*), as implemented in scanpy (1.4.5) (*71*) to approximate differentiation and maturation processes. After transferring the data to a scanpy object, we used the Harmony-corrected components to construct a graph based on the 20 nearest neighbors of each cell. A diffusion map was computed based on the neighborhood graph and was used as input for pseudotime estimated with zero branchings. The root of the pseudotime was specified as a random cell belonging to the earliest timepoint and from a cluster characterized by the expression of precursor marker genes for the respective cell type (e.g., *Atoh1* in granule cells, *Ptf1a* in interneurons). Specifically for the interneurons, where multiple subtypes are specified at different developmental stages (fig. S13E-F), we observed that pseudotime values above 0.6 captured subtype rather than differentiation signal. Since the aim of this analysis was to describe differentiation paths common to all interneuron subtypes, we capped pseudotime values to 0.6, and then rescaled them from 0 to 1 (fig. S13C).

To identify dynamic features, pseudotime values were divided into 50 bins based on their ranks and cells belonging to the same bin were grouped together. The CRE accessibility, gene scores and chromVAR-derived motif deviations profiles were aggregated across cells within each pseudotime bin. Dynamic features across pseudotime were identified based on mutual information between the feature (scaled CRE accessibility, gene score, chromVAR deviation score) and the mean pseudotime of each bin using the function cminjk.pw() from the R package mpmi (*72*). Cutoffs for maximum mutual information index

(MMI) were determined based on empirical null distributions obtained by shuffling the pseudotime values across bins (controlling for an FDR < 1%). Furthermore, as the MMI distribution was often bimodal, we used a Gaussian mixture model, as implemented in the R package mclust (5.4.5) (*73*) to split the distribution into two groups. Features belonging to the group with the highest MMI and passing the 1% FDR cutoff were identified as significantly dynamic. Significantly dynamic CREs were Z-score standardized and clustered based on their pseudotemporal profiles using a fuzzy c-means clustering algorithm for time series from the R package Mfuzz (2.46.0) (*70*). The optimal number of clusters was determined by generating an elbow plot for the minimum distance between cluster centroids, as well as by monitoring the trajectory profile and gene ontology enrichment of each cluster (reducing the number of clusters when multiple clusters shared similar trajectories and gene ontology enrichment).

For the integrative analysis of neuronal differentiation we identified CREs with dynamic activity in more than one neuron type (pleiotropic). We visualized activity patterns of pleiotropic CREs across neuron types with a chord diagram from the R package circlize (*74*) (Fig. 4E) where each node represents a CRE and connects its activity clusters across two neuron types. The significance of the overlap between CRE clusters from different cell types was assessed with hypergeometric tests. For the principal component analysis (PCA), we generated pseudobulks per cell type and pseudotime bin, applied a variance stabilizing transformation as implemented in the package DESeq2 (1.26) (*65*) and performed PCA as implemented in the package FactoMineR (*75*).

Transcription factors with dynamic activity in cell type differentiation

The aggregated accessibility of CREs containing a given TF motif can be used to infer the activity of the TF in a given cell type and state. Compared with assessing the activity of the TF using gene expression data (RNA-seq), this metric allows the detection of changes in activity driven by posttranslational modifications, such as phosphorylation or interactions with co-factors. However, TFs that belong to the same family often recognize very similar motifs, hindering the precise identification of the specific TF

that is driving the observed change in chromatin accessibility. To overcome this limitation we used an integrative approach to identify TFs with dynamic motif accessibility and gene score (as a proxy for gene expression) across cell type differentiation. We identified significantly dynamic motifs and gene scores based on the MMI estimated from the 50 pseudotime bins (see "*Cell type differentiation"*). We further estimated Pearson's correlations between motif activity and gene scores across pseudotime (using the average values in the 50 bins). We then identified candidates for the regulation of cell type differentiation as TFs that 1) reached a minimum gene score of 1.5 in at least one pseudotime bin, 2) showed dynamic chromVAR deviation score and 3) gene score, and 4) showed an absolute correlation coefficient of $r > 0.6$ between the motif accessibility and gene score. TFs were then classified as putative activators or repressors depending on the sign of the correlation coefficient between gene score and motif accessibility akin to similar analyses by others (*76*). Information on TF families was obtained from cisBP (Build 2.0) (*59*).

CRE evolutionary dynamics

To compare CRE evolutionary dynamics across cell types and developmental stages, we calculated summary statistics per cell based on all intergenic CREs accessible in that cell. As described above (see *"Peak annotation"*), for each CRE we inferred its minimum age, estimated the average sequence constraint in its most conserved 100 bp region, and calculated the fraction of the CRE covered by genomic repeats. For each cell, we calculated the mean values for these estimates across all intergenic CREs that were accessible in that cell. We focused these analyses on intergenic elements, to avoid biases from overlaps with or proximity to protein-coding sequences, which overall show very high sequence conservation, often independently of regulatory constraint. Due to the sparsity of snATAC-seq data, these estimates vary across single cells, even within the same cell type and state. To estimate summary statistics for groups of cells (e.g., as shown in Fig. 5), we only considered estimates based on at least 50 cells and calculated the mean value for each biological replicate. The variance in these estimates between biological replicates is shown in the error bars.

For the contributions of different age groups and of transposable element classes to the regulatory landscape of different cell types we estimated per cell the fraction of accessible intergenic CREs in each class (inferred age or overlapping transposable element class) over the total number of accessible intergenic CREs in that cell. The absolute value of this estimate depends on the overall abundance of such elements in the mouse genome (e.g., fraction of fragments in B1 elements is much higher than ERVs), but we observed additional variation between cell types and stages (Fig. 5B and fig. S17B-C). For the comparison between CREs associated with TFs versus other genes, we considered all protein-coding genes assigned to at least one intergenic CRE and estimated the average constraint/age of all intergenic CREs assigned to each gene. Genes corresponding to TFs were obtained from AnimalTFDB v3 (*77*). The significance of these comparisons between groups was assessed with two-sided Mann-Whitney *U* tests.

Temporal differences in granule cell differentiation

To distinguish between differentiation (inferred by pseudotime) and developmental stage contributions towards the conservation of the *cis*-regulatory landscape of granule cells we used a linear model with both pseudotime and developmental stage as predictors of average CRE constraint per cell (as described in *"CRE evolutionary dynamics"*). The significance of each predictor term was estimated using ANOVA tests between the full model and an alternative model that excluded that term.

For temporal differences in the prenatal granule cell progenitors we extracted cells from stages E13-P0 that belonged to the same cluster (cluster 4), prior to any Harmony-correction across developmental stages or pseudotime inference (fig. S13A left and fig. S16E). Thus, in this analysis we considered cells that overall look the most similar to each other based on their raw chromatin accessibility profiles. We generated pseudobulks per sample (developmental stage and biological replicate), considered CREs with at least 10 counts in at least two samples and applied the variance stabilizing transformation as implemented in DESeq2 (1.26) (*65*). We then detected temporally dynamic CREs using masigPro (1.58.0) with a second degree polynomial and requiring a Benjamini-Hochberg adjusted *P*-value < 0.05

and a goodness of fit value $R^2 > 0.7$ (*78*). For temporally dynamic CREs, we estimated the mean accessibility across replicates, performed a Z-score standardization across developmental stages and applied soft clustering with k=2 using Mfuzz (2.46.0) (*70*). We examined the activity of each cluster in the rest of the dataset by estimating the fraction of CPM in these CREs per cell. To assess the impact of these temporal differences on gene expression, we considered the genes that were closest to these CREs, excluding genes that were associated with CREs from both clusters. We then examined the expression of these genes in a scRNA-seq atlas of mouse cerebellum development (*23*) focusing on the cells annotated as "Embryonic and postnatal GCPs-1", as described for temporally variant genes (see *"Identification of temporally-variant genes in progenitors"*). We used proximity instead of our correlation-based gene assignment approach to avoid the circularity of examining the concordance between gene expression and chromatin accessibility after requiring them to be correlated.

Opossum snATAC-seq processing and CRE identification

Opossum snATAC-seq data were processed as described for mouse with following modifications: we generated a custom reference for cellranger and ArchR using the genome build monDom5 from Ensembl v96 (*56*). Since the first two chromosomes in the opossum genome are very long, which causes errors in many bioinformatics tools, we split them at position 536141000, making sure that no gene is interrupted in this process. Remaining segments from chromosomes 1 and 2 were named "chr1b" and "chr2b" respectively. These modified coordinates were used for all analyses, but for table S7 we also report the original monDom5 coordinates. For gene annotation, we supplemented the Ensembl annotation with a set of lncRNAs expressed during opossum development (*40*).

For processing in ArchR, we retained cells with at least 5,000 fragments (as in mouse) but reduced the requirement for TSS enrichment to 2 (from 3) as TSS annotations are less precise in the opossum genome. Putative doublets were removed in two steps: first in ArchR with a doublet ratio of 1.0, then manually by removing all cells with a doublet enrichment score > 4 or with more than 2.5 times the

median number of fragments in the library. LSI projection was performed as described for mouse, but we additionally used Harmony (*50*) as implemented in ArchR to correct the embedding as we observed small differences between replicates. The Harmony-corrected embedding was used for UMAP projection and Louvain clustering with a resolution of 1.0 (due to the smaller number of cell types and states compared to the mouse atlas which covers the entire cerebellum development). Cell type annotation was performed on the basis of shared marker genes with the mouse (using gene scores; fig. S18A). Clusters 15 and 16 were further subclustered to split P21 differentiating granule cells and UBCs, which were identified as a distinct subcluster with high gene score activity for *Lmx1a*.

Putative CREs were identified in a cluster-specific and replicate-aware manner as described for mouse. Since we subsequently used the opossum CREs to assess regulatory conservation in mouse, we capped each group (cluster and replicate) to a maximum of 200 cells and a maximum of 5,000,000 fragments to limit the effect of cell type abundances on our conservation estimates. Additionally, only peaks accessible in at least 5% of the cells in a cluster were included in the "robust CRE" set and considered for downstream analyses (as in mouse). Genomic annotation of CREs was performed in ArchR based on the combined Ensembl and lncRNA annotation (see above).

Regulatory activity conservation between mouse and opossum

We used reciprocal syntenic alignments to identify conserved CREs between mouse and opossum. Specifically, we used liftOver with a minimum match of 0.1 (minimum overlap of 50 bp) to identify syntenic regions for the CREs of "species A" to the genome of "species B". We then used bedtools intersect (2.29) (*57*) to overlap these syntenic regions with the CRE annotation of "species B". Thus, we identified CREs from one species that are syntenic to CREs in the other species. We then only retained reciprocal matches. Nearly 75% of those matches were in 1:1 relationships (a single mouse CRE matched a single opossum CRE). Since we used a fixed width for our CREs, we also considered an additional 12% of cases where a single CRE in one species matched two CREs in the other species, which were adjacent

to each other (up to 500 bp apart). In those cases we retained the CRE with the highest overlap. Additional one-to-many and many-to-many matches were excluded from downstream analyses.

To compare regulatory activity conservation across cell types and developmental stages, we only considered mouse samples from P4 and P63, which based on transcriptomic similarity are the corresponding stages to the opossum samples (*39*). For each cell in the mouse we estimated the fraction of accessible intergenic CREs that have a CRE ortholog in opossum. We then grouped these estimates by cell type, state and developmental stage, akin to our sequence conservation analyses. Additionally, we assessed conservation of CRE activity in the same cell type and stage. To this end, we aggregated CRE accessibility profiles of opossum cells across cell types and stages and identified the 40,000 most accessible CREs per group (approximately corresponding to the 5 CPM cutoff we used in other analyses as a binary cutoff for CRE activity). For each mouse cell, we estimated the fraction of accessible intergenic CREs with an opossum CRE ortholog in the 40,000 most accessible CREs in the corresponding cell type and stage.

To assess cell type and stage correspondences, we focused on orthologous CREs, intergenic in both species. We aggregated accessibility profiles across cells from the same cell type and developmental stage and scaled for sequencing depth (in CPM, before subsetting for intergenic CREs). We ordered the accessibility matrices in the same way in both species (using the orthologous intergenic CREs) and estimated rank-based Spearman's correlations across cell types and stages. To estimate the degree of conservation of spatiotemporal activity for each pair of orthologous intergenic CREs, we calculated Pearson's correlation coefficients of their CPM-scaled accessibility across matched samples (corresponding cell types and developmental stages), which we compared to correlations between pairs of intergenic CREs with shuffled homology relationships.

General statistics and visualization

All statistical analyses were performed in R (3.6.3) (*79*) using the packages tidyverse (1.3.0) (*80*), data.table (1.12.8) (*81*), Matrix (1.2.18) (*82*), SummarizedExperiment (1.16.1) (*83*), irlba (2.3.3) (*84*) and cluster (2.1.0) (*85*). Heatmaps were drawn using the packages ComplexHeatmap (2.2.0) (*86*) and pheatmap (1.0.12) (*87*). Additionally, we used the R packages shiny (1.4.0.2) (*88*), shinyjs (1.1) (*89*), Gviz (1.30.3) (*90*) and GenomicInteractions (1.20.3) (*91*) to build the app that facilitates the interactive exploration of our data.

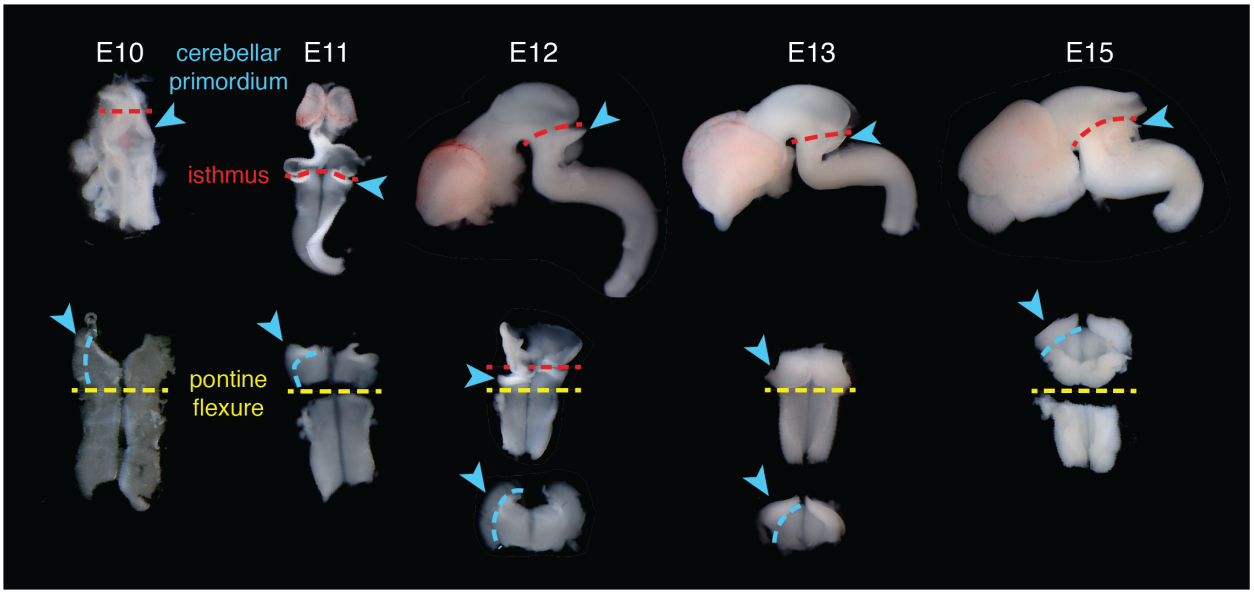

Fig. S1. Dissection of fetal cerebellar primordia.

Example stereomicroscope images for embryos from different developmental stages (E10-E15) are shown. The brains were dissected and most of meninges were removed (top row). The brains were cut at the isthmus (red lines) and then at the pontine flexure (bottom row, yellow line) to isolate the prepontine hindbrain. The roof of the hindbrain was opened, the neural tube was flattened and the cerebellar primordia (blue arrowheads) were dissected as the two regions of the alar plate on each side of the flattened tissue. Images are not to scale.

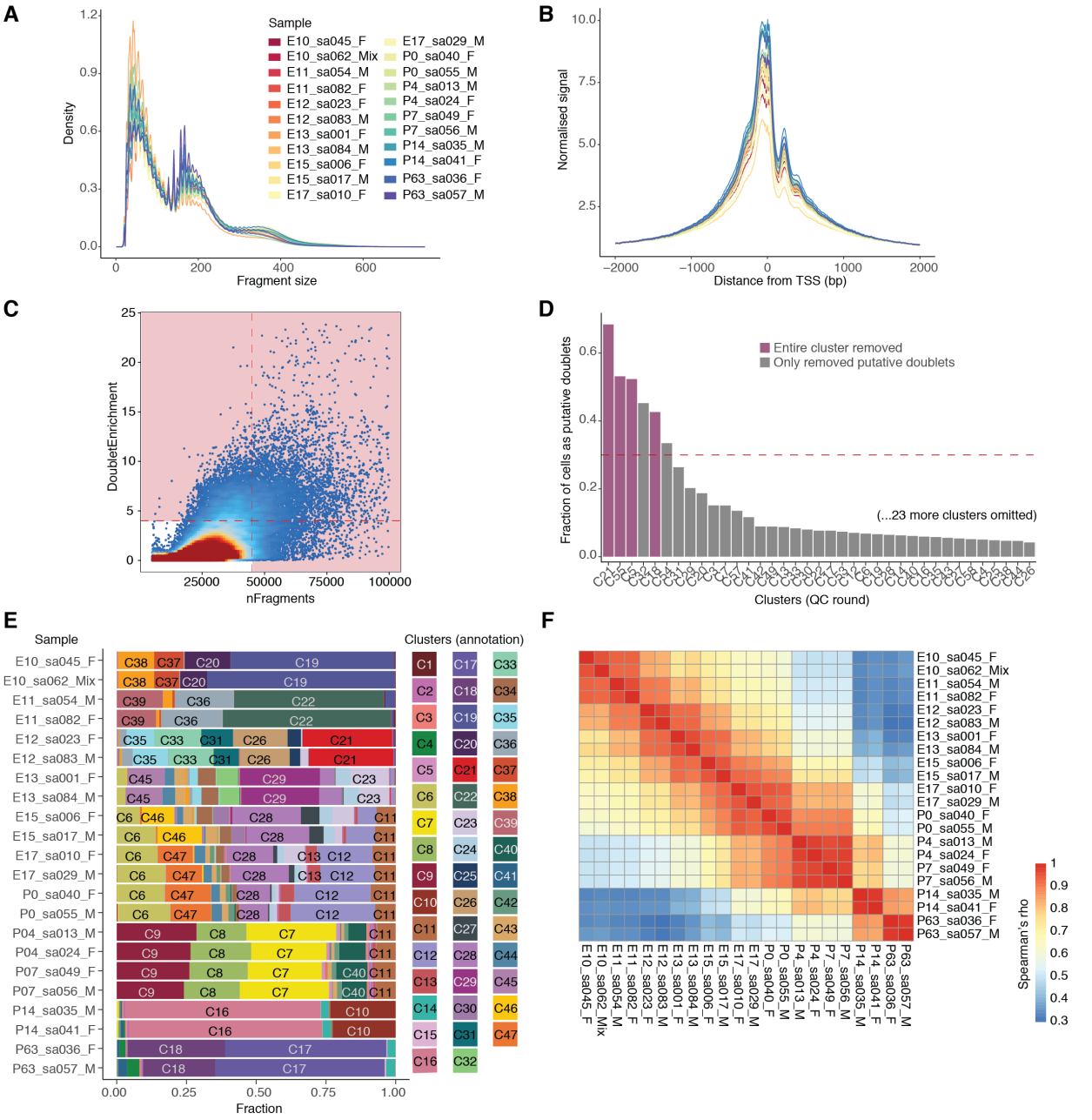

Fig. S2. Quality control of snATAC-seq data.

(A) Fragment size distribution of the snATAC-seq libraries, labeled by developmental stage, library code and sex (F: female; M: male; Mix: pooled embryos from both sexes). **(B)** Transcription start site (TSS) enrichment scores of the snATAC-seq libraries. **(C)** 2D-density plot showing the number of fragments and doublet enrichment score per cell after 1st pass removal of putative doublets. Cells in red-shaded areas were removed in the 2nd round of doublet filtering. **(D)** Fraction of cells marked as doublets in the 2nd filtering round per cluster. Clusters with more than 30% of doublets (horizontal line) were manually examined for marker genes. Clusters marked in violet were removed completely. For all other clusters (gray) only putative doublets were removed. **(E)** Fraction of cells in each cluster by snATAC-seq sample.

(F) Spearman's rho correlation coefficients across samples (snATAC-seq libraries). Counts in autosomal CREs (see fig. S7) were aggregated across all cells in each sample and scaled by sequencing depth (in counts per million, CPM). Correlations were estimated based on the ranks of CPM values within each sample. Samples are ordered by developmental stage.

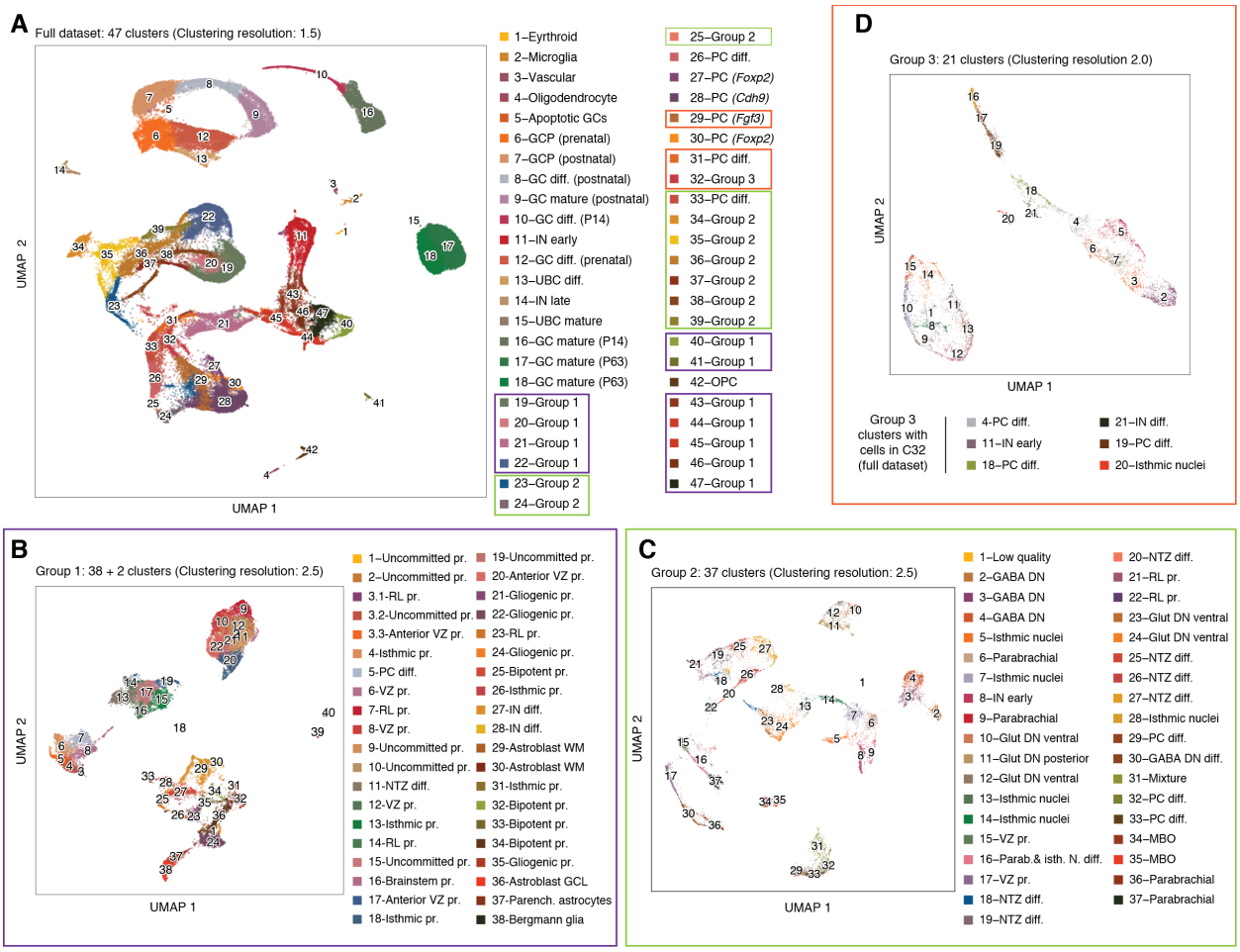

Fig. S3. Iterative clustering for cell type annotation.

(A) UMAP projection of 91,922 high quality cells colored by cluster assignment. Clusters that could not be resolved were combined in three groups (labeled as Group 1-3). Some annotated clusters (i.e., clusters 29, 31 and 33) were included in these groups to aid the split and annotation of the mixed clusters. The colored rectangles indicate which clusters were used for subclustering within each group. **(B, C, D)** UMAP projections of subclustering analyses for astroglia (Group 1; B), early-born neurons (Group 2; C) and GABAergic neurons at E13 (Group 3; D). Abbreviations: diff.: differentiating; GABA DN: GABAergic deep nuclei neurons; GC: granule cells; GCL: granule cell layer; GCP: granule cell progenitors; Glut DN: glutamatergic deep nuclei neurons; IN: GABAergic interneurons; MBO: midbrain originating cells; NTZ: nuclear transitory zone; OPC: oligodendrocyte progenitors; Parab. & isth. N. diff. : parabrachial and isthmic nuclei differentiating neurons; Parench: Parenchymal; PC: Purkinje cells; pr.: progenitor; RL: rhombic lip; UBC: unipolar brush cells; VZ: ventricular zone; WM: white matter.

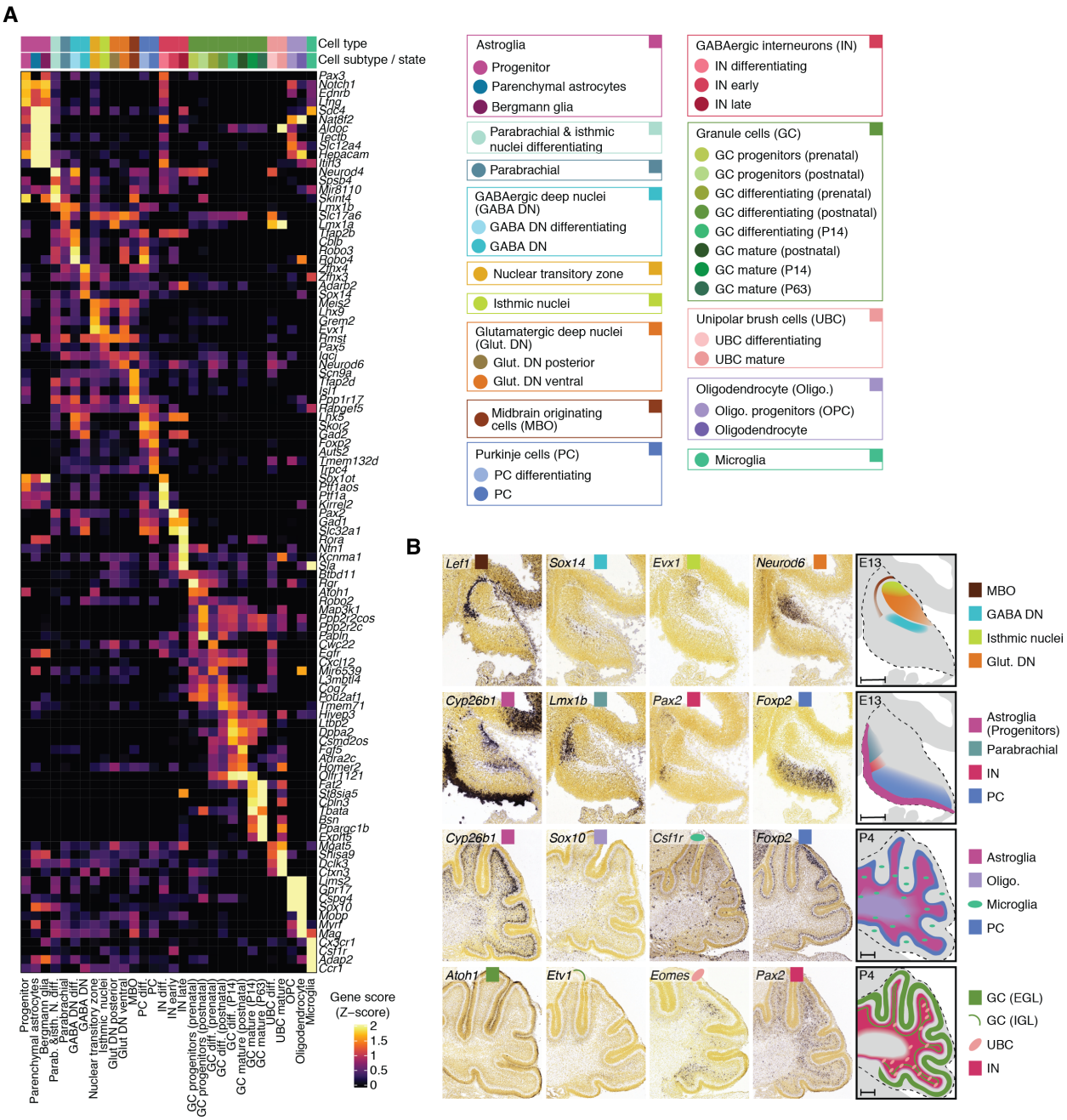

Fig. S4. Marker genes across cell types and states.

(A) Activity scores of top 4 marker genes per cell type or state (Z-score, capped to 0-2). Marker genes were identified using Wilcoxon tests, as implemented in ArchR, and ranked based on the product of their $\log_2$ fold-change estimate and the $-\log_{10}$ *P*-value of the test. Grouping of cell states or subtypes (circles) into broad cell types (rectangles) is shown on the right. **(B)** *In situ* hybridization images from Allen Developing Mouse Brain Atlas (*49*) for selected cell type marker genes in E13 or P4 mouse cerebellum. Sagittal sections counterstained with HP Yellow (left) and a schematic summary of cell type localization (right) are shown. Scale bars: 200 µm. Abbreviations as in A; EGL/IGL: external/internal granule cell layer.

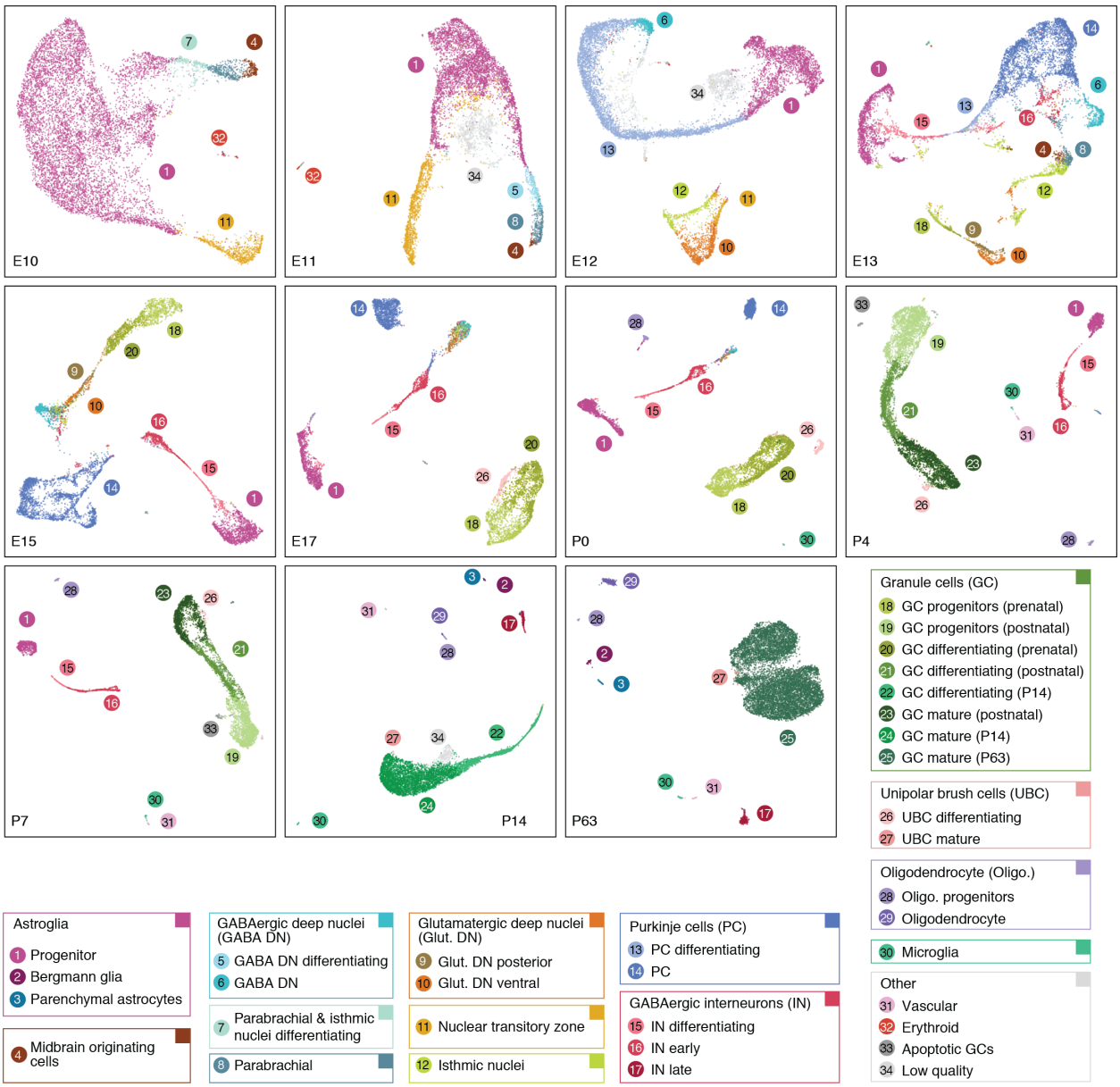

Fig. S5. Cell type annotations by developmental stage.

UMAP projections of individual developmental stages colored by cell type and state. Cell states or subtypes (numbered circles) are grouped together into broad cell types (rectangles). Further division of progenitors and interneurons into subtypes is shown in Fig. 3, fig. S11 and S13.

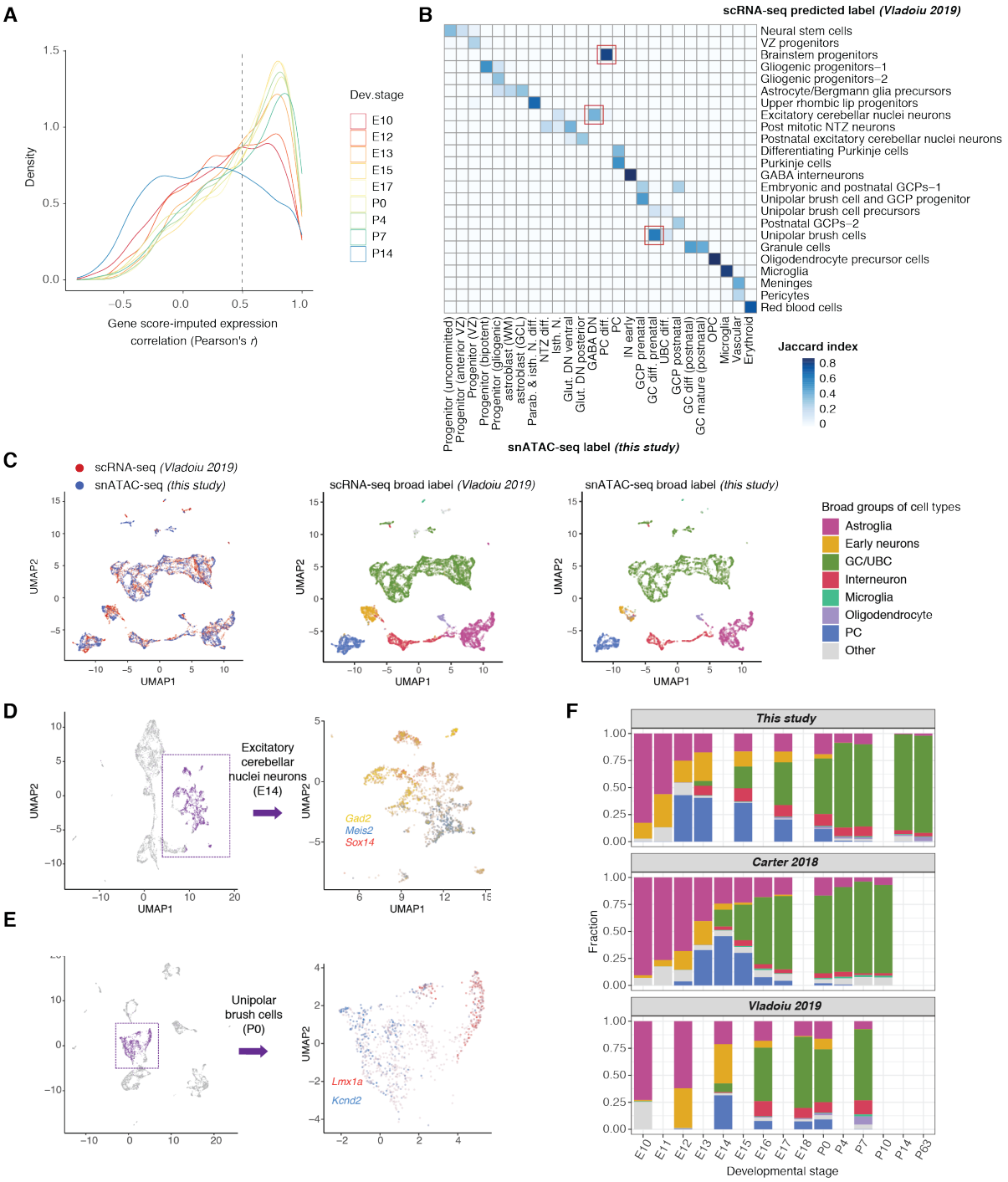

Fig. S6. Comparison with scRNA-seq data.

(A) Per gene correlation (Pearson's *r*) between gene score and imputed expression (after integration with scRNA-seq data from Vladoiu et al. 2019 (*23*)) for highly variable genes in the scRNA-seq data. For each developmental stage, gene scores and imputed expression values were averaged within each snATAC-seq cluster. For each highly variable gene in the scRNA-seq data, gene score values across clusters were correlated with the imputed expression values across clusters. The vertical line indicates the median correlation coefficient across developmental stages. **(B)** Jaccard similarity index between cell type labels from this study (columns) and

predicted labels after integration with scRNA-seq data (rows). Only labels with a similarity index of at least 0.15 with at least one other group are shown. The red rectangles mark the unexpected matches of (i) differentiating Purkinje cells (PC diff.) in our dataset to brainstem progenitors in the scRNA-seq dataset, (ii) GABAergic deep nuclei neurons (GABA DN) to excitatory (glutamatergic) cerebellar nuclei neurons, and (iii) prenatal differentiating granule cells (GC diff. prenatal) to unipolar brush cells. In the case of the first mismatch involving differentiating Purkinje cells we detect activity for Purkinje cell markers, such as *Skor2* and *Lhx5*, no signal of progenitor markers, such as *Notch1* (see fig. S4A) or for lower brainstem markers including *Hox* genes (*3*). The two latter mismatches are driven by the presence of heterogeneous cell populations in the scRNA-seq data as shown in D and E. **(C)** UMAP projection of P0 cerebellum cells profiled with scRNA-seq (*23*) and snATAC-seq (this study) co-embedded based on real and imputed expression. Cells from both datasets (left and middle) are colored by modality (left) or broad cell type groups from (*23*) (middle). Broad cell type groups assigned in this study are shown for the cells from the snATAC-seq atlas (right). Cell types were grouped into broad categories to facilitate comparisons between studies that differ in annotation strategies and resolution. **(D)** UMAP projection of 6,068 cells from E14 cerebellum profiled by scRNA-seq (*23*) with cells annotated by the authors as excitatory cerebellar nuclei neurons marked in purple (left). Further examination of this group for the expression of glutamatergic deep nuclei and isthmic nuclei neurons marker *Meis2* (blue), GABAergic neurons marker *Gad2* (yellow), and GABAergic deep nuclei neurons marker *Sox14* (red) (*92*), suggests that the scRNA-seq cluster contains a mixture of both glutamatergic and GABAergic deep nuclei neurons (right). **(E)** UMAP projection of 4,809 cells from P0 cerebellum profiled by scRNA-seq (*23*) with cells annotated by the authors as unipolar brush cells (UBCs) marked in purple (left). Only a fraction of these cells are positive for the UBC marker *Lmx1a* (red) (*93*), and a sizeable group of the cells expresses the granule cell marker *Kcnd2* (blue) (right). RNA expression matrices and cell type annotations were obtained from (*23*). **(F)** Proportions of broad cell type groups across developmental stages in our snATAC-seq atlas (top), and scRNA-seq atlases by Carter et al. 2018 (*27*) (middle) and Vladoiu et al. 2019 (*23*) (bottom). Cell types were grouped into broad categories to facilitate comparisons between the three studies that differ in annotation strategies and resolution. diff.: differentiating, DN: deep nuclei, GC: granule cell, GCL: granule cell layer, GCP: granule cell progenitor, IN: interneuron, OPC: oligodendrocyte progenitor cell, PC: Purkinje cell, VZ: ventricular zone, WM: white matter.

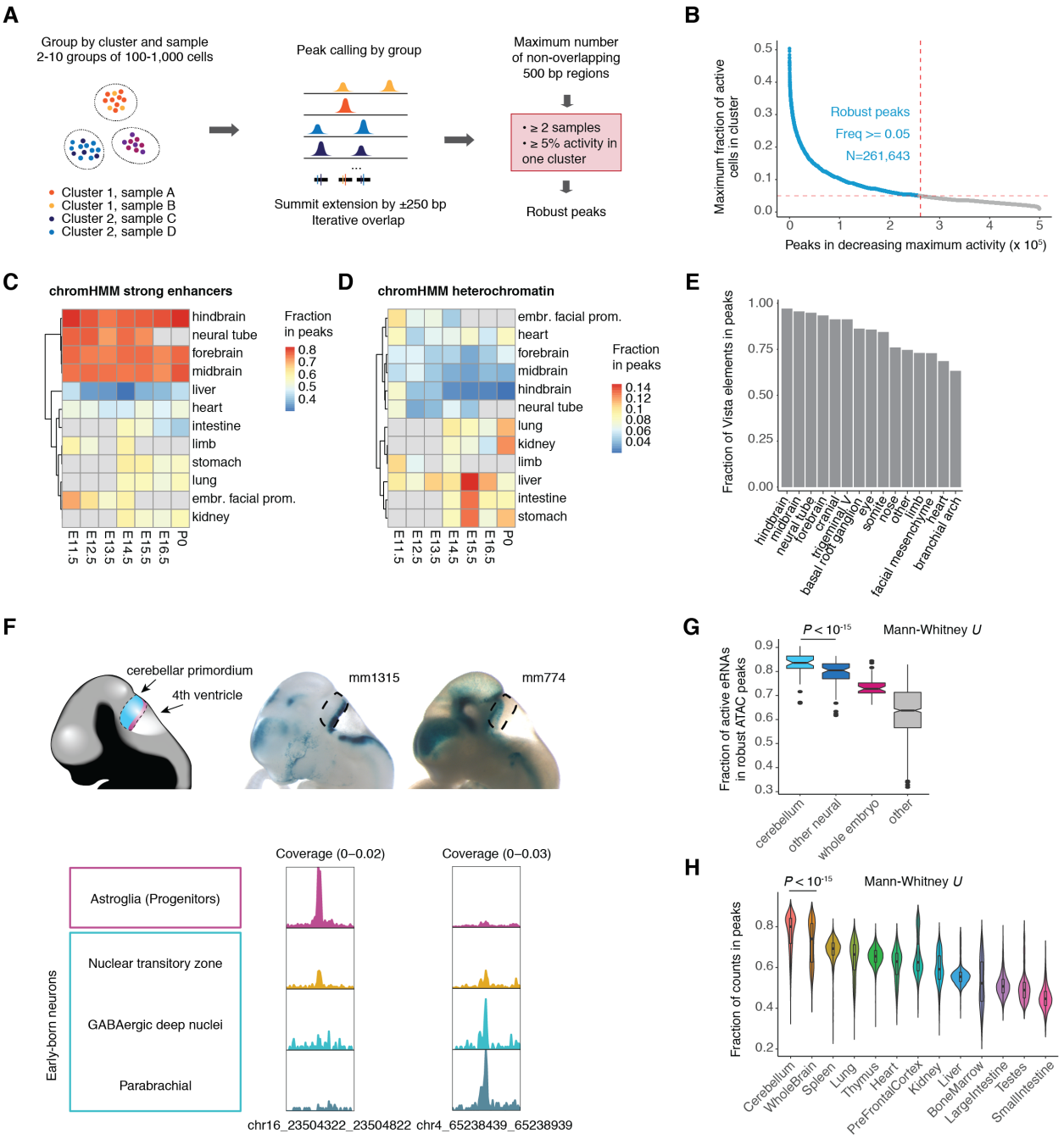

Fig. S7. CRE identification and comparison to other datasets.

(A) Schematic representation of the procedure followed for the identification and filtering for putative CREs. **(B)** Putative CREs ranked based on their maximum activity across clusters (fraction of cells with at least one fragment in that CRE in the cluster with maximum activity). Robust CREs were identified as active in at least 5% of the cells of at least one cluster. **(C, D)** Fraction of chromHMM predicted strong enhancers (C) and heterochromatin (D) across a series of tissues and developmental stages (*11*) recalled in the robust CRE set from this study. Gray values: data not available. **(E)** Fraction of experimentally validated enhancers in mouse embryonic tissues (*28*) overlapping robust CREs from this study. Tissues are ordered by

decreasing fraction. **(F)** Examples of experimentally validated enhancers recovered in this study. Top: *LacZ* reporter stainings in whole-mount E11 embryos from VISTA Enhancer Browser (*28*) for two elements with activity in the progenitors (mm1315; signal visible in the rhombic lip) and early-born postmitotic neurons (mm774; signal visible in the cerebellar mantle zone). The cerebellar primordium and relative positions of progenitors and postmitotic neurons are marked in the scheme on the left. Bottom: Aggregated snATAC-seq accessibility profiles (scaled by the total number of fragments in each group) across cell types in E11 for CREs overlapping the elements shown on top. **(G)** Fraction of expressed enhancer RNAs (eRNAs) recalled in the robust CRE set from this study across samples from the developing cerebellum, other neural tissues, whole embryo development and all other mouse samples from (*29*). **(H)** Per-cell fraction of fragments in regions overlapping robust CREs from this study across different organs in the adult mouse (*15*). Tissues are ordered by decreasing median fraction across cells.

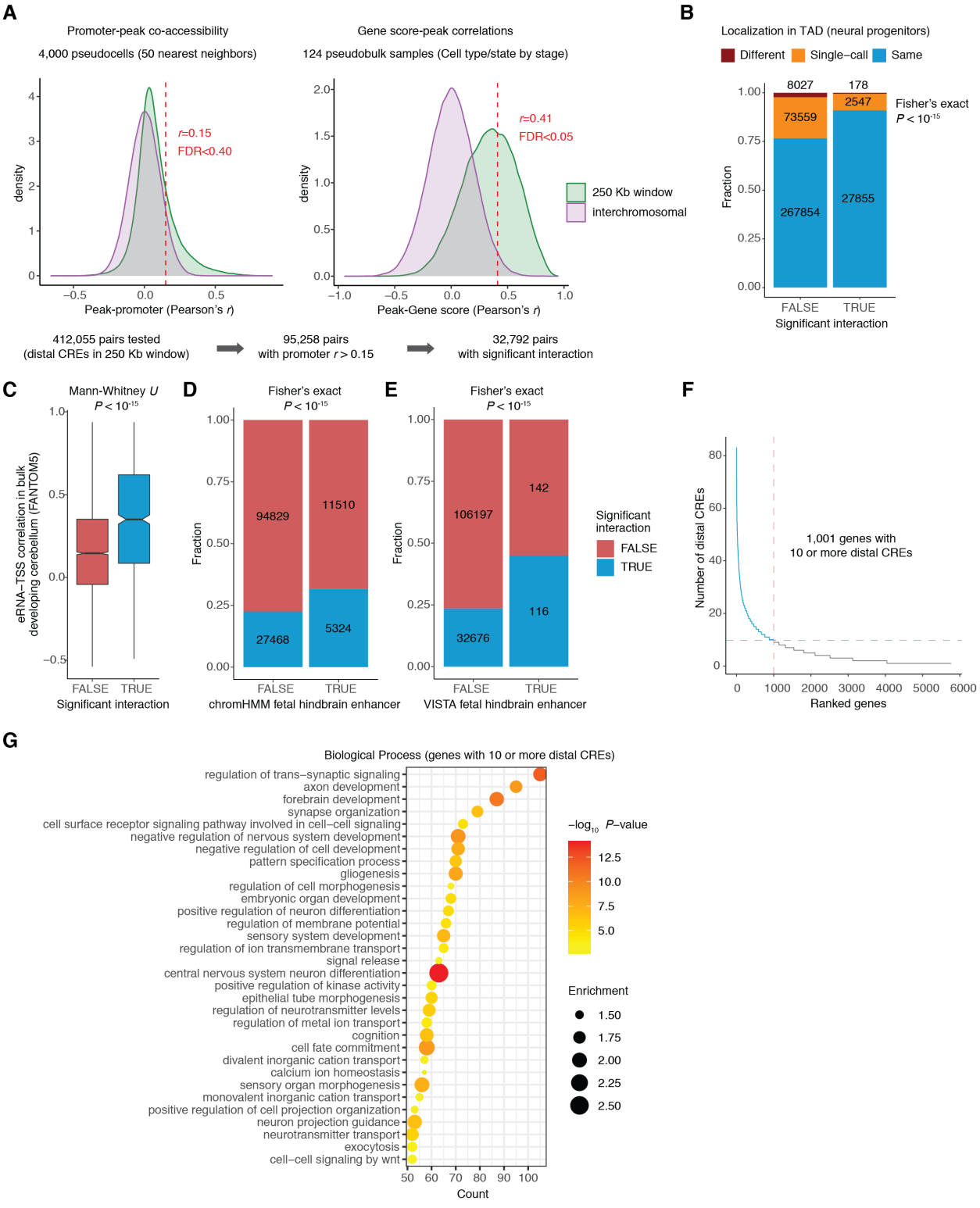

Fig. S8. Assignment of CREs to putative target genes.

(A) Correlation-based assignment of distal CREs to putative target genes. Left: Pearson's correlation coefficients between distal CRE and promoter accessibility in 250 kb windows

(green) or across different chromosomes (purple). Fragment counts per CRE were aggregated across ~4,000 random groups of 50 nearest neighbors, scaled by sequencing depth, log-transformed and used as input to compute correlations across pseudocell profiles. Right: Pearson's correlation coefficients between distal CRE accessibility and gene score for CRE-gene pairs with a promoter-peak correlation of $r \geq 0.15$ (left, maximum correlation for genes with multiple promoters) in 250 kb windows (green) or across different chromosomes (purple). CRE accessibility and gene score estimates were aggregated across groups by cell type/state and developmental stage (124 pseudobulk samples with at least 40 cells). Estimates were scaled by sequencing depth, log-transformed and used to compute correlations across pseudobulks. Interchromosomal correlations were used to construct a null correlation and significant CRE-gene interactions were identified with $r \geq 0.41$ (BH adjusted $P < 0.05$). **(B)** Fraction of distal CRE-promoter pairs in the same (blue) or different (red) topologically associating domain (TAD) in mouse neural progenitors (*30*) stratified by significance of interaction between CRE-promoter pairs. Single-call (orange): only one region was assigned to a TAD. **(C)** Pearson's correlation coefficients between the expression of enhancer RNAs (eRNAs), overlapping distal CREs from this study, and promoter associated RNAs at transcription start sites (TSS) across cerebellum development (*29*) stratified by significance of interaction between CRE-promoter pairs. **(D, E)** Fraction of distal CREs assigned to a gene for elements overlapping putative enhancers in hindbrain development (*11*) (D) or experimentally validated enhancers in the E11 hindbrain (*28*) (E). **(F)** Genes ranked in decreasing order by the number of distal CREs assigned to them. **(G)** Biological process enrichment for genes associated with 10 or more distal CREs (from F). The x-axis indicates the number of genes associated with each term, the size and color of the dots the effect and significance of the enrichment based on a hypergeometric test.

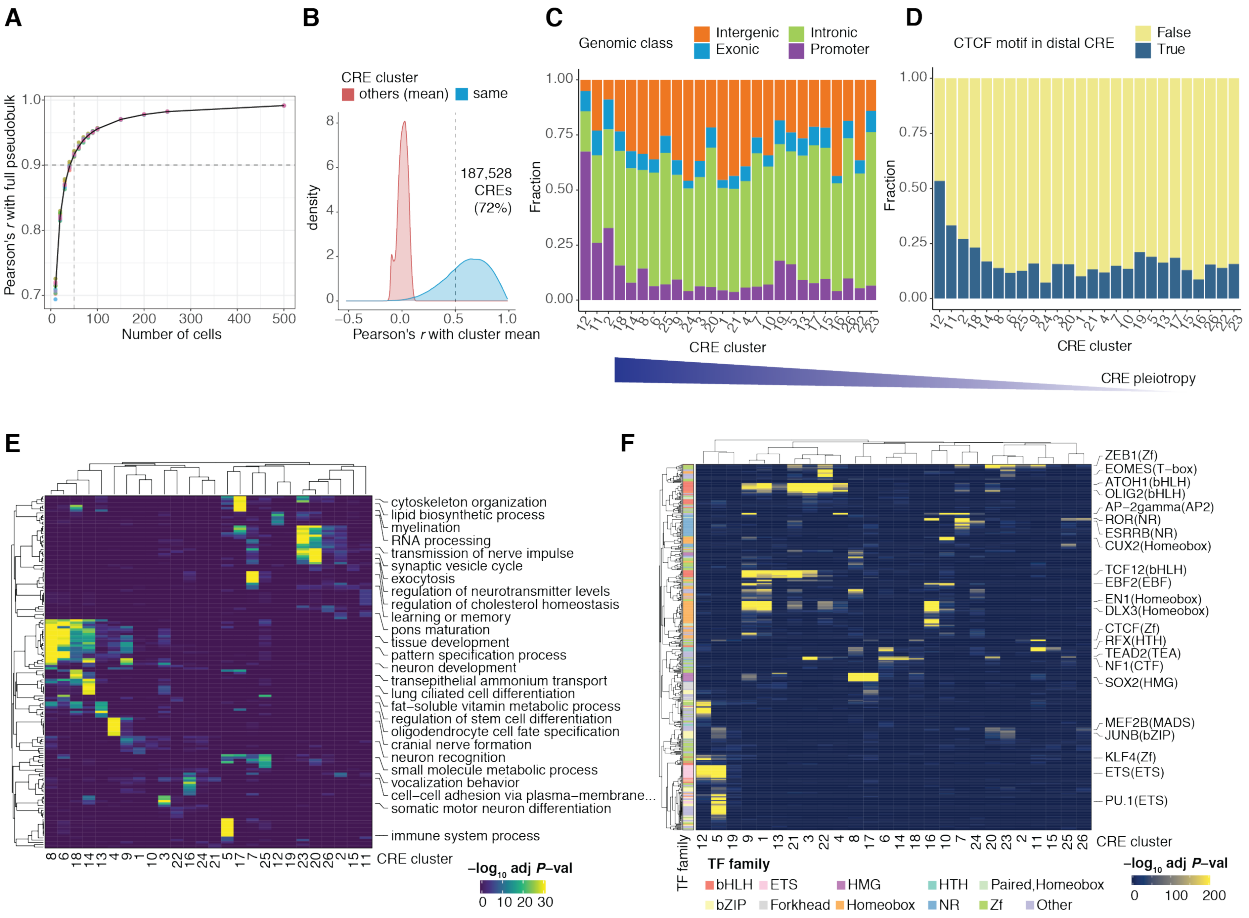

Fig. S9. Characterization of CRE clusters.

(A) Subsampling analysis in P63 granule cells (library sa036). CRE accessibility was aggregated across randomly sampled pseudobulks of different cell numbers and correlated with the aggregated accessibility of all 4,964 granule cells in the sample. Subsampling was repeated ten times (colors). The black line shows the mean correlation across the ten subsampling analyses. The vertical line marks pseudobulks of 50 cells, which are the smallest cell population sufficient for a correlation greater than 0.9 (horizontal line). **(B)** Distribution of Pearson's correlation coefficients between each CRE and its associated cluster center from Fig. 2B (average of all CREs in that cluster; blue) compared to the average correlation of each CRE with the centers of all other clusters. Correlations were estimated based on standardized CRE accessibilities across cell types and developmental stages. CREs with $r > 0.5$ (vertical line) were identified as high-confidence members of their clusters. **(C)** Fraction of genomic classes across clusters of CREs, indexed and ordered as in Fig. 2B. **(D)** Fraction of distal CREs overlapping at least one CTCF motif across clusters of CREs, indexed and ordered as in Fig. 2B. **(E, F)** Enrichment of biological processes of adjacent genes (E) and TF motifs (F) across clusters of CREs, indexed as in Fig. 2B (BH adjusted $P < 0.05$; hypergeometric test).

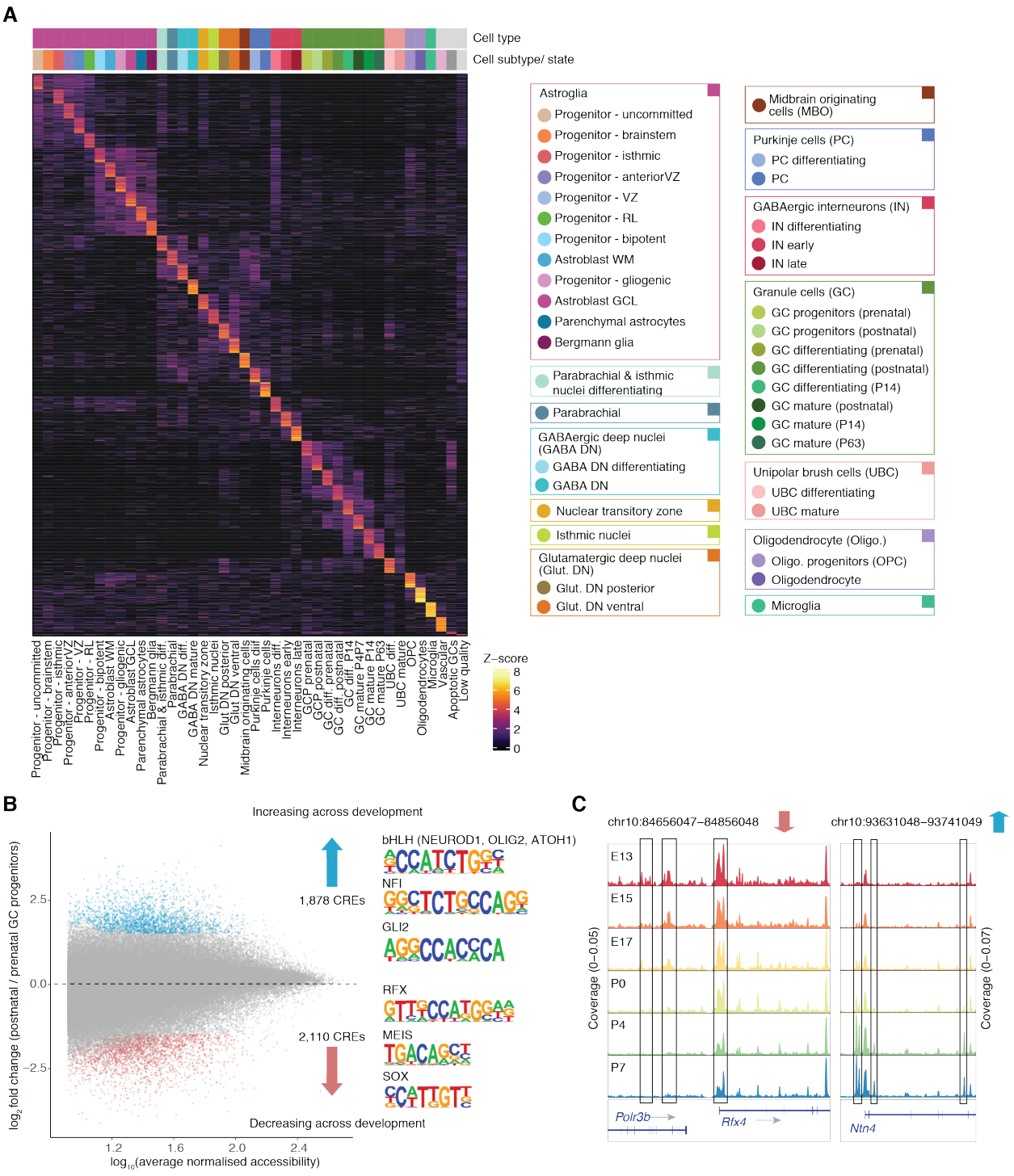

Fig. S10. Cell type and state-specific CREs.

(A) Activity scores of the top 50 differentially accessible CREs per cell type and state (Z-score, capped to 0-8). Differentially accessible CREs were identified using Wilcoxon tests as implemented in ArchR and ranked based on the product of their $\log_2$ fold-change estimate and the $-\log_{10}$ *P*-value of the test. Grouping of cell states or subtypes (circles) into broad cell types (rectangles) is shown on the right. **(B)** MA plot of differentially accessible CREs between pre-

and postnatal granule cell progenitors. CRE accessibility was aggregated within each cell state and sample (replicate), variance stabilized and used as input for differential accessibility analysis in DESeq2 (*65*). CREs with significantly increased (blue) and decreased (red) accessibility in postnatal compared to prenatal granule cell progenitors were identified with an absolute $\log_2$ fold-change of at least 1.5 and a BH adjusted *P*-value < 0.05. TF motifs with highest enrichment based on hypergeometric tests are shown for each group. **(C)** Examples of aggregated accessibility profiles (scaled by the total number of fragments in each group) across granule cell progenitors of different developmental stages for CREs with decreasing (left) and increasing (right) accessibility during development. Abbreviations: GCL: granule cell layer; RL: rhombic lip; VZ: ventricular zone; WM: white matter.

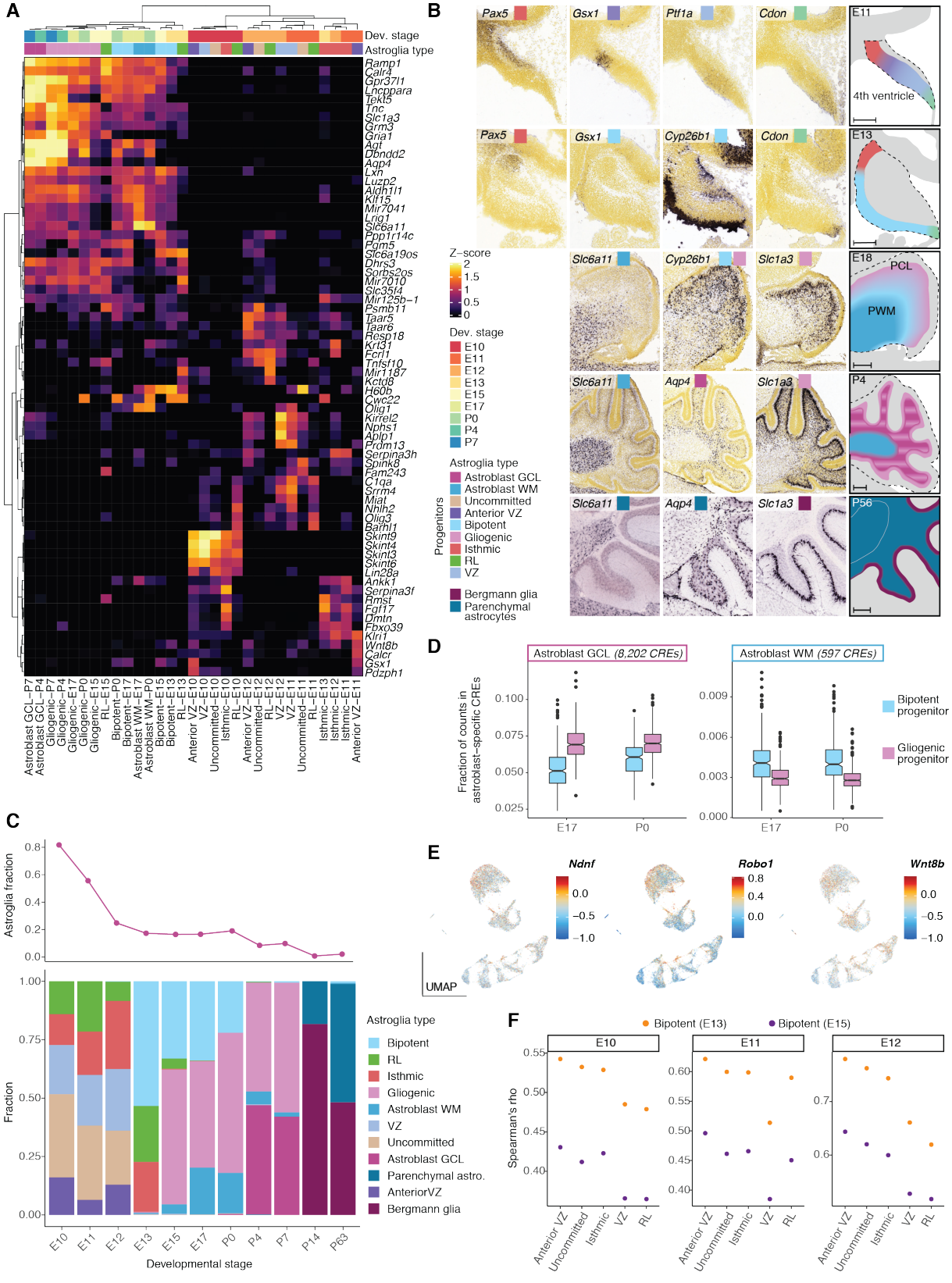

Fig. S11. Annotation of progenitor types. ***See legend on next page.***

Fig. S11. Annotation of progenitor types.
(A) Gene scores of the top 4 marker genes per astroglia type or state (Z-score, capped to 0-2). Marker genes were identified using Wilcoxon tests as implemented in ArchR and ranked based on the product of their $\log_2$ fold-change estimate and the $-\log_{10}$ *P*-value of the test. **(B)** Estimated localization of astroglia types in the developing mouse cerebellum (right) based on *in situ* hybridization data (*49*) of selected marker genes (left). Sagittal sections counterstained with HP Yellow (E11-P4) or Nissl (P56) are shown. Early (E11, E13) progenitor populations locate next to the 4^{th} ventricle, whereas late (E18, P4) bipotent and gliogenic progenitors migrate to the prospective white matter and developing Purkinje cell layer, respectively (*2*, *36*). Scale bars: 200 μm. **(C)** Relative abundance of astroglia types (bottom) and overall fraction in the cerebellum (top) across developmental stages. **(D)** Comparison of granule cell layer and white matter astroblasts to E17 and P0 bipotent and gliogenic progenitors. Fraction of fragments per cell in CREs specific to astroblast populations across progenitor types and developmental stages. Different y-ranges were used across CRE sets to facilitate comparisons between progenitor groups as the overall fraction of fragments depends on the number of CREs in each set. All comparisons between progenitor groups are significant ($P < 10^{-15}$, Mann-Whitney *U* tests). **(E)** Gene scores for marker genes that are shared between anterior VZ and bipotent progenitors (counts per 10^4 fragments, capped at 10th and 99th quantiles and $\log_{10}$ transformed). **(F)** Spearman's correlation coefficients based on all CREs between early (E10-E12) progenitor types and bipotent progenitors from E13 (orange) and E15 (purple). Fragment counts were aggregated across all cells from a progenitor type and developmental stage, scaled by sequencing depth and used as input for rank-based correlations between groups. Different y-ranges were used across stages to facilitate comparisons between progenitor types from the same stage as correlations decrease with increasing developmental distance. Abbreviations: GCL: granule cell layer; PCL: Purkinje cell layer; PWM: prospective white matter; RL: rhombic lip; VZ: ventricular zone; WM: white matter.

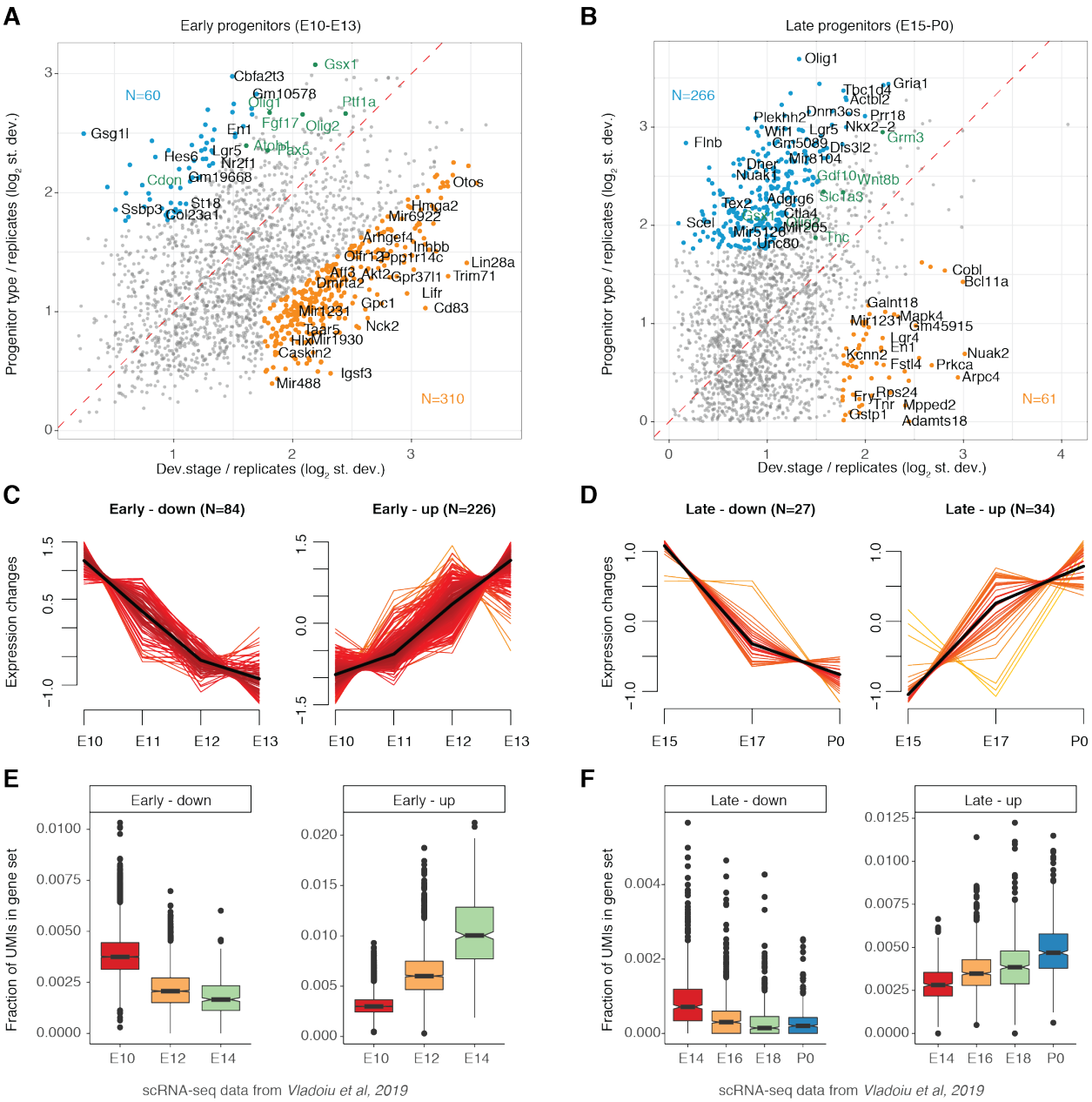

Fig. S12. Identification of temporally-variant genes in progenitors.

(A, B) Log_2 ratio of standard deviations across developmental stages (x-axis) and progenitor types (y-axis) over mean standard deviation between replicates, for the 2,000 genes with highest gene score variance for early (E10-E13; A) and late (E15-P0; B) progenitor populations. Gene scores were averaged across groups from the same progenitor type, developmental stage and replicate. Variance across these groups was used to select the 2,000 most variant genes. Standard deviations were then computed per gene for the mean values across progenitor types or developmental stage. Standard deviations across replicates refer to the mean standard deviation across groups of the same progenitor type and developmental stage and different replicate. Temporally-variant (orange) genes and germinal zone-variant (blue) genes were identified with a log_2 ratio of at least 1.25 compared to both other standard deviations. Marker genes used for the

identification of progenitor types are shown in green. **(C, D)** Z-score scaled gene score for temporally-variant genes (orange in A, B) for early (E10-E13; C) and late (E15-P0; D) progenitor populations with decreasing (left) and increasing (right) activity, as determined by fuzzy clustering. The number of genes in each cluster is shown on top. **(E, F)** Fraction of UMIs per progenitor cell in temporally-variant genes clusters from C, D**.** Data and annotations are from Vladoiu et al. 2019 (*23*). Different y-ranges were used across gene sets to facilitate temporal comparisons within each group as the overall fraction of UMIs depends on the number of genes in each set.

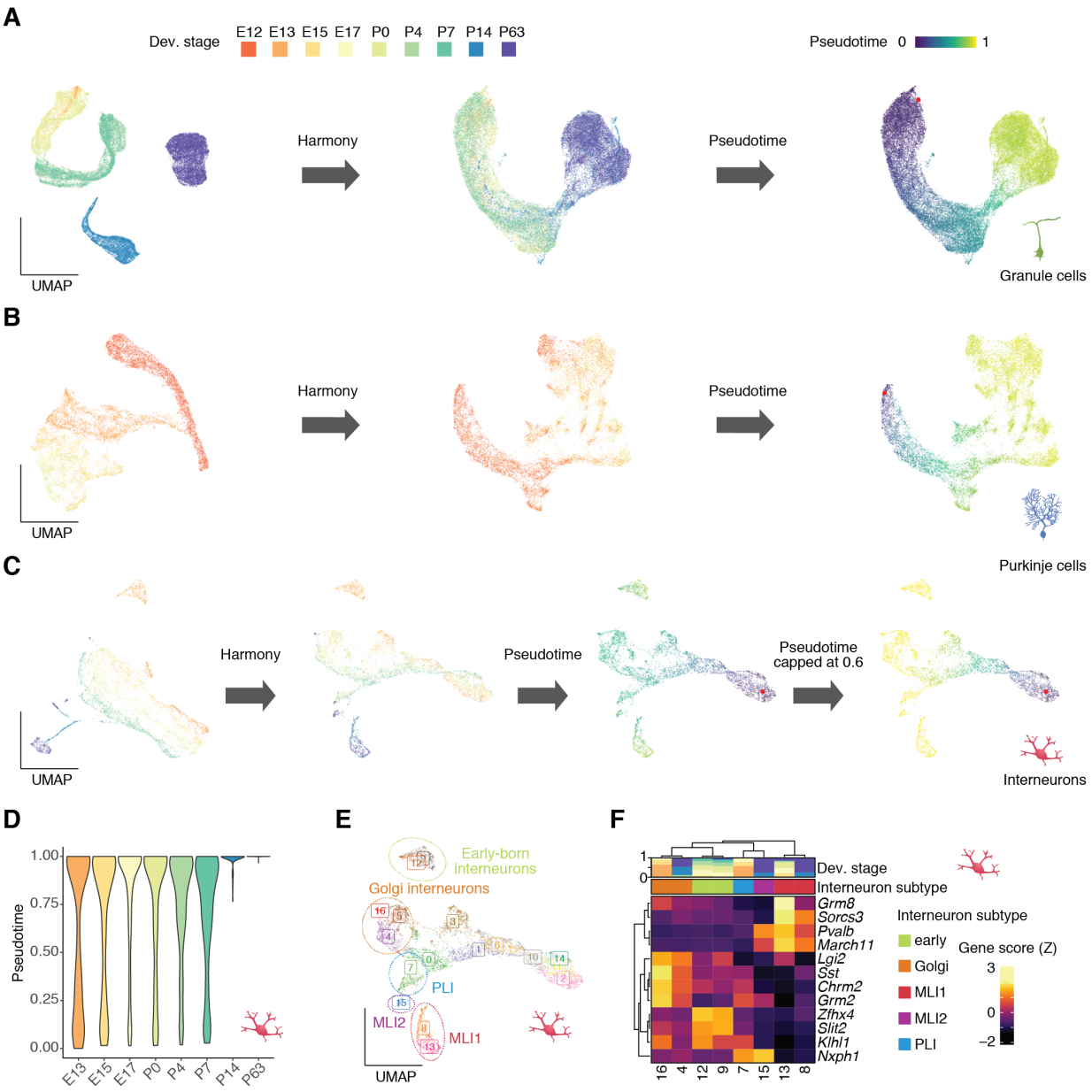

Fig. S13. Modeling of neuron differentiation.

(A, B, C) UMAP projections of 35,153 granule cells (A), 13,214 Purkinje cells (B) and 5,113 interneurons (C) before (left) and after (middle and right) Harmony-alignment across developmental stages. Cells are colored by developmental stage (left and middle) and pseudotime value (right). For interneurons (C), pseudotime was capped at 0.6 and rescaled to eliminate differences between temporally specified subtypes (see E, F). **(D)** Distribution of pseudotime values (after capping) across developmental stages for interneurons. **(E)** UMAP projection of 5,113 Harmony-aligned interneurons colored by cluster. Temporally specified interneuron subtypes are shown in circles. **(F)** Gene score activity (Z-score) of marker genes for mature interneuron clusters (as in E). Subtype annotation and relative contribution of developmental stages per cluster are shown above the heatmap. Abbreviations: MLI: molecular layer interneurons; PLI: Purkinje layer interneurons.

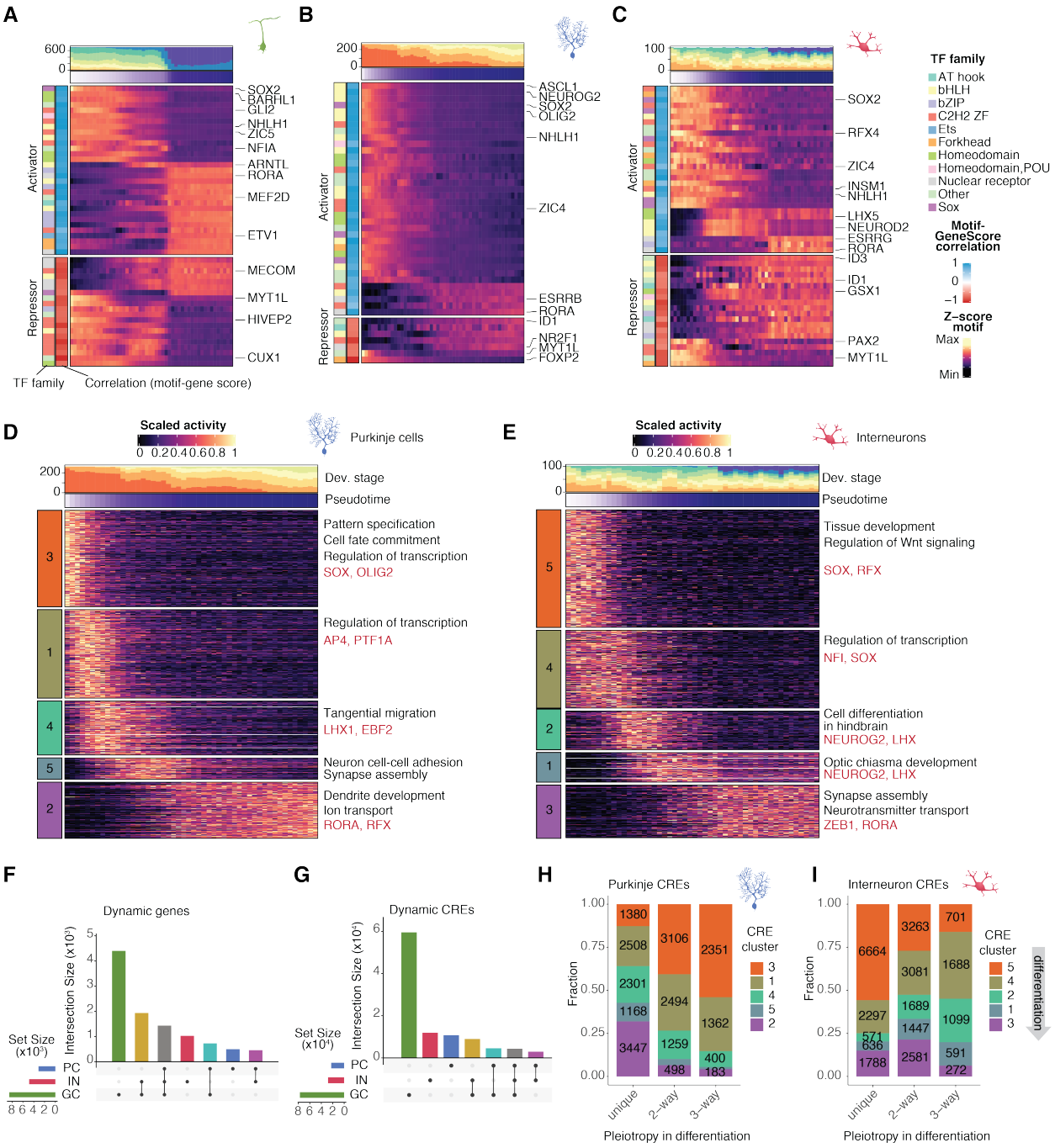

Fig. S14. Chromatin accessibility dynamics during neuron differentiation.

(A, B, C) Z-score scaled motif accessibility for TFs with dynamic activity across differentiation of granule cells (A), Purkinje cells (B) and interneurons (C). Cells were grouped in 50 bins based on pseudotime ranks and motif scores were averaged within each group. Top: Contribution of developmental stages and mean pseudotime value for each bin. Left: TF family and Pearson's correlation between motif accessibility and gene score. TFs with positive or negative correlations are classified as putative activators (blue) and repressors (red) respectively and ordered from early to late activity based on their gene scores. **(D, E)** Z-score scaled activity of dynamic CREs across differentiation of Purkinje cells (D) and interneurons (E). Cells were grouped in 50 bins

based on pseudotime ranks and CRE counts were aggregated across cells within each group and scaled by sequencing depth. Top: Contribution of developmental stages and mean pseudotime value for each bin. Right: Representative enrichments (BH adjusted $P < 0.05$; hypergeometric test) for biological processes of adjacent genes (black) and TF motifs (red). CRE clusters (left) are ordered from early (orange) to late (violet) activity during differentiation. **(F, G)** Upset plots of intersections between genes (F) and CREs (G) with dynamic activity in differentiating granule cells, Purkinje cells and interneurons. Connected dots mark overlapping sets. Horizontal bars (bottop) show the total number of dynamic genes (F) and CREs (G) per cell type. **(H, I)** Fraction of CRE clusters (as in D, E and ordered from early (orange) to late (violet) activity during differentiation) across CREs dynamic in a single neuron type (unique) or shared across two or three cell types, for Purkinje cells (H) and interneurons (I).

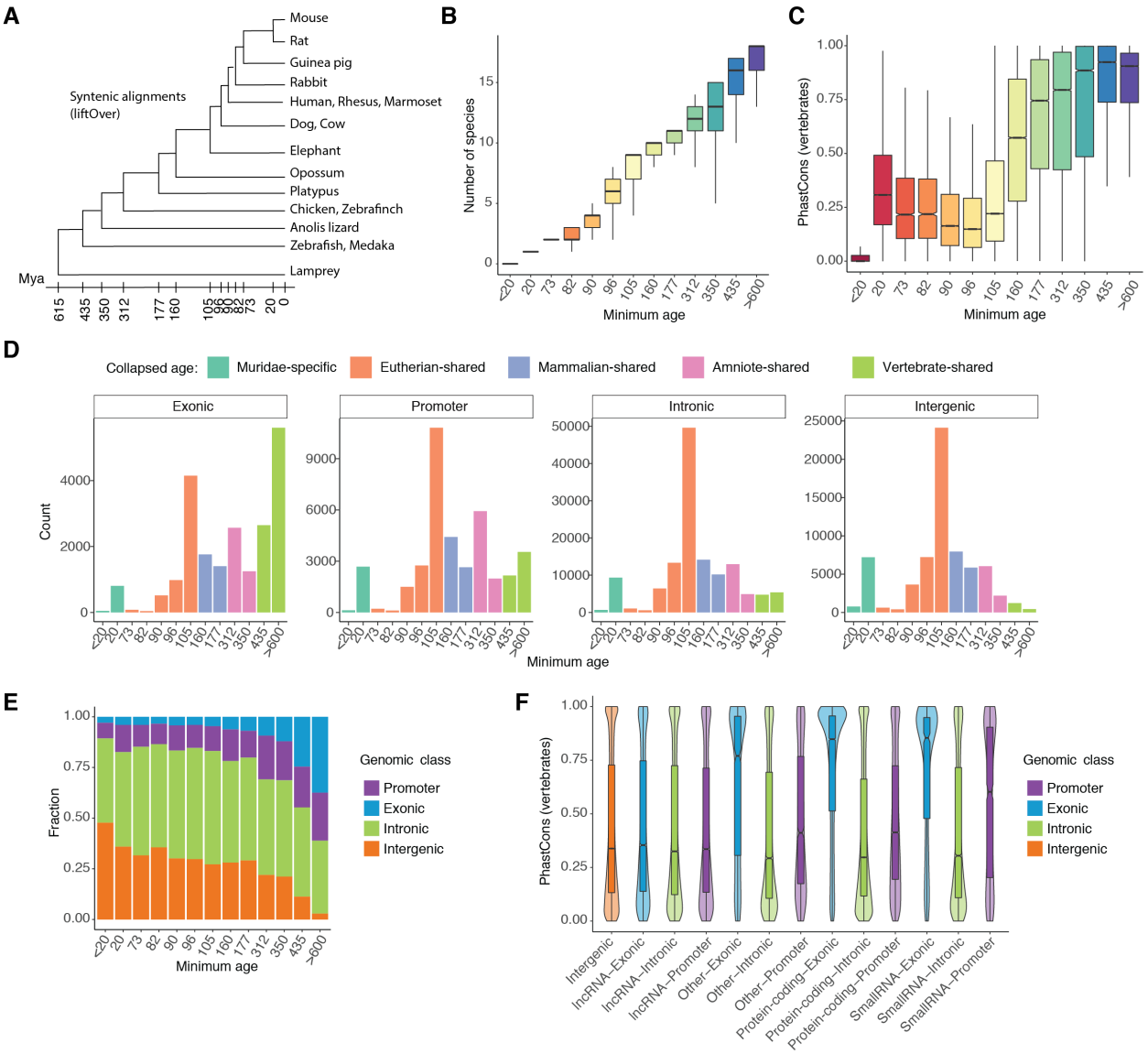

Fig. S15. Evolutionary characterization of CREs.

(A) Species used in the syntenic alignments to infer the minimum age of CREs based on the date of divergence (from *timetree.org*) between mouse and the most distant species in which an alignment was detected. Mya: Million years ago. **(B)** Number of species in which a syntenic alignment was detected for CREs of different inferred ages. **(C)** Sequence constraint for CREs of different ages. **(D)** Number of CREs across genomic classes and age groups. Colors indicate broader age groups as used in Fig. 5B. **(E)** Relative representation of genomic classes across CRE age groups. **(F)** Sequence constraint for CREs of different genomic classes.

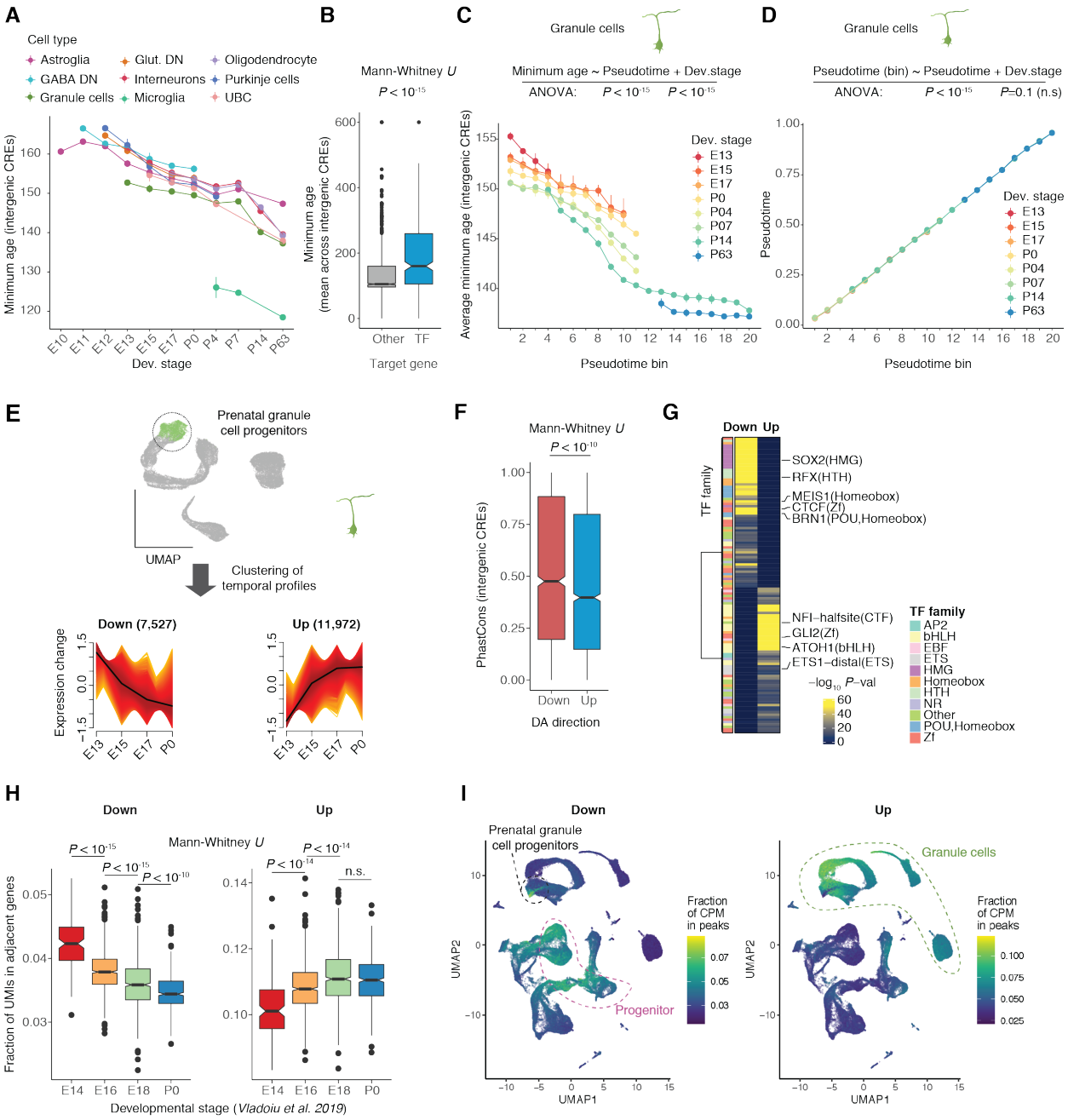

Fig. S16. CRE conservation during development and differentiation.

(A) Minimum age of intergenic CREs accessible per cell, averaged for each cell type and developmental stage. Vertical bars illustrate the difference in average estimates between biological replicates. **(B)** Average minimum age of intergenic CREs per gene for TFs and other genes. **(C, D)** Minimum age of intergenic CREs (C) and pseudotime (D) per cell, averaged for each developmental stage (color) and pseudotime interval (step=0.05) of granule cell differentiation. Vertical bars illustrate the difference in average estimates between biological replicates. **(E)** Identification of temporal differences in CRE activity in prenatal granule cell progenitors (top; UMAP of 35,153 GCs prior to alignment across developmental stages, as in S13A). Z-score scaled temporal activity of CREs with decreasing or increasing accessibility

across development (bottom). Black lines indicate mean values for each cluster. **(F, G)** Sequence constraint (F) and TF motifs enrichment (G; BH adjusted $P < 0.05$; hypergeometric test) for intergenic CREs with temporal differences in prenatal granule cell progenitors (clusters from E). **(H)** Fraction of UMIs per cell in putative target genes of CREs with decreasing (left) or increasing (right) accessibility during development in prenatal granule cell progenitors. Data and annotations are from Vladoiu et al. 2019 (*23*). Different y-ranges were used across gene sets to facilitate temporal comparisons within each group as the overall fraction of UMIs depends on the number of genes in each set. **(I)** Fraction of counts per million (CPM) per cell in CREs with decreasing (left) or increasing (right) accessibility during development in prenatal granule cell progenitors (from E). GABA DN: GABAergic deep nuclei neurons; Glut. DN: glutamatergic deep nuclei neurons; UBC: unipolar brush cells.

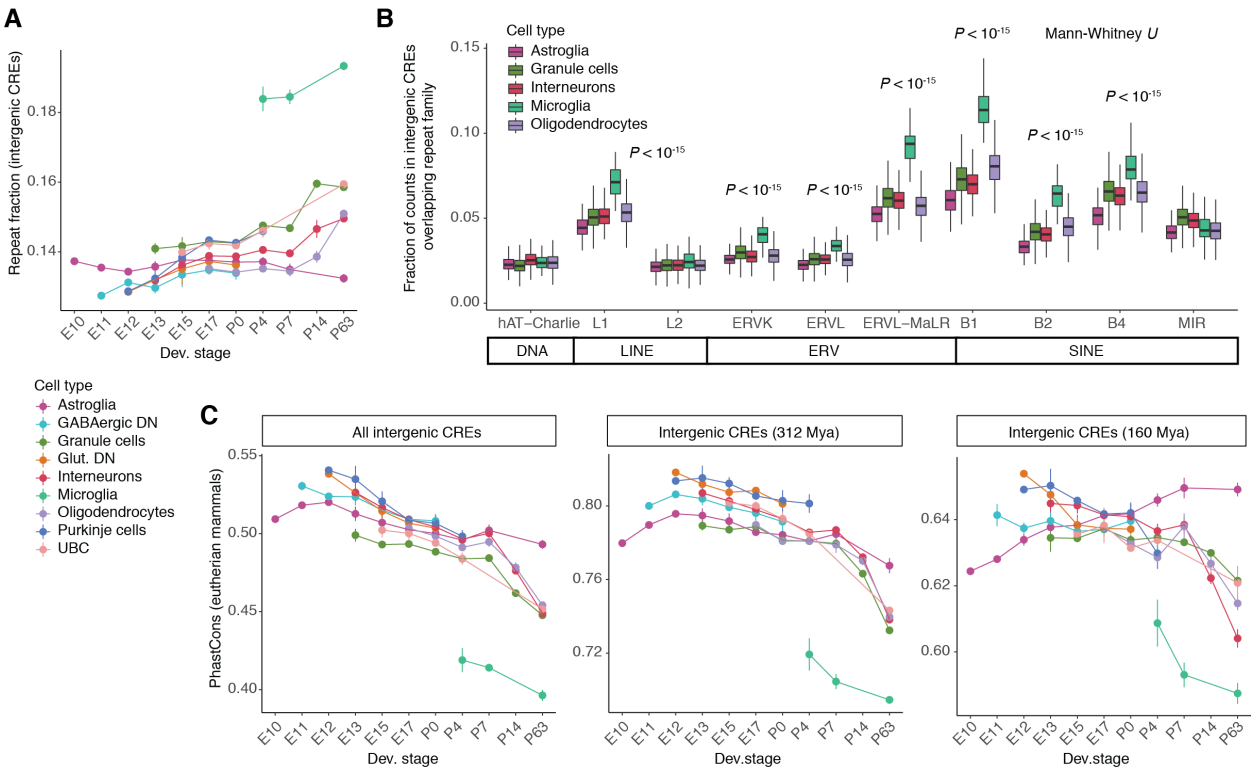

Fig. S17. Contributions to cell type differences in constraint.

(A) Fraction of fragments in intergenic CREs accessible per cell overlapping repeats, averaged for each cell type and developmental stage. **(B)** Fraction of fragments in intergenic CREs accessible per cell overlapping transposable elements of different classes, grouped by cell types of the adult mouse cerebellum (P63). **(C)** Sequence constraint across eutherian (commonly referred to as placental) mammals for all intergenic CREs (left), and subsets that originated 312 (middle) and 160 (right) million years ago (Mya) accessible per cell, averaged for each cell type and developmental stage. Different y-ranges were used across age groups to facilitate comparisons between cell types and stages within each group, as sequence constraint is overall higher for older CREs. In A and C, vertical bars illustrate the difference in average estimates between biological replicates. DN: deep nuclei neurons; Glut.: glutamatergic.

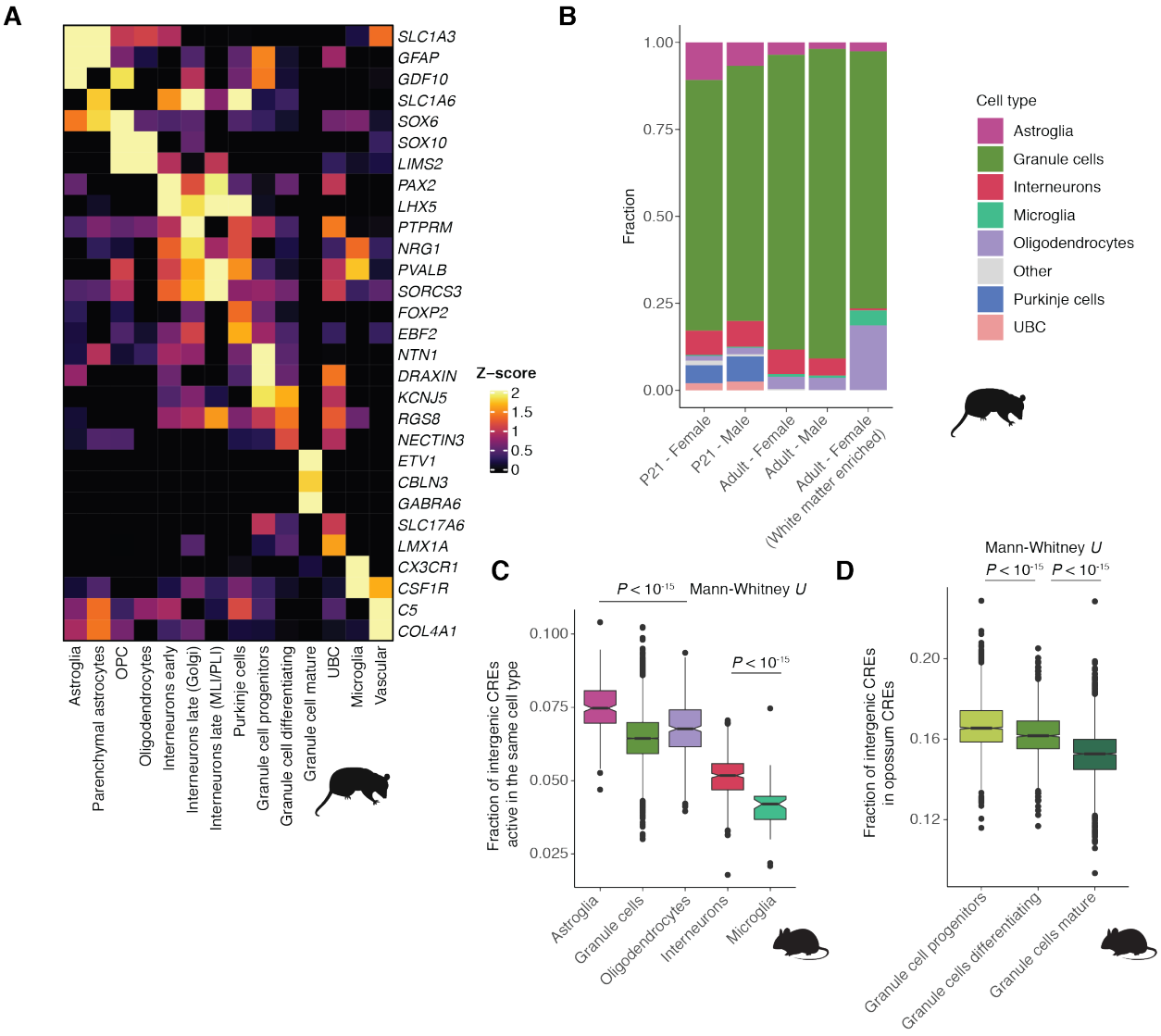

Fig. S18. Opossum snATAC-seq data and comparisons with mouse.

(A) Activity scores of genes used for the annotation of opossum cell types and states (Z-score, capped to 0-2). **(B)** Proportions of broad cell types across samples. **(C)** Fraction of intergenic CREs, accessible per cell in adult mouse, with an ortholog in the 40,000 most accessible CREs of the corresponding cell type in the adult opossum (after aggregating counts across all cells in that cell type and scaling by sequencing depth). **(D)** Fraction of intergenic CREs, accessible per cell in P4 mouse, with an ortholog CRE in opossum, grouped by differentiation state of granule cells (as in Fig. 1C). MLI: molecular layer interneurons; OPC: oligodendrocyte progenitors; PLI: Purkinje cell layer interneurons; UBC: unipolar brush cells.

Captions for Tables S1 to S7

Table S1. (separate file)
Information on sample dissections, library preparation and statistics

Table S2. (separate file)
Clustering, cell type annotation and summary statistics of high quality cells.

Table S3. (separate file)
Distal CREs assigned to putative target genes.

Table S4. (separate file)
Temporally-variant genes in cerebellar progenitor populations.

Table S5. (separate file)
TFs associated with the differentiation of major cerebellar neuron types.

Table S6. (separate file)
Software and external resources used in this study.

Table S7. (separate file)
Intergenic CREs shared between mouse and opossum.

References and Notes

1. A. Sathyanesan, J. Zhou, J. Scafidi, D. H. Heck, R. V. Sillitoe, V. Gallo, Emerging connections between cerebellar development, behaviour and complex brain disorders. *Nat. Rev. Neurosci.* **20**, 298–313 (2019).
2. K. Leto, M. Arancillo, E. B. E. Becker, A. Buffo, C. Chiang, B. Ding, W. B. Dobyns, I. Dusart, P. Haldipur, M. E. Hatten, M. Hoshino, A. L. Joyner, M. Kano, D. L. Kilpatrick, N. Koibuchi, S. Marino, S. Martinez, K. J. Millen, T. O. Millner, T. Miyata, E. Parmigiani, K. Schilling, G. Sekerková, R. V. Sillitoe, C. Sotelo, N. Uesaka, A. Wefers, R. J. T. Wingate, R. Hawkes, Consensus Paper: Cerebellar Development. *Cerebellum*. **15**, 789–828 (2016).
3. T. Butts, M. J. Green, R. J. T. Wingate, Development of the cerebellum: simple steps to make a 'little brain.' *Development*. **141**, 4031–4041 (2014).
4. A. S. Nord, A. E. West, Neurobiological functions of transcriptional enhancers. *Nat. Neurosci.* **23**, 5–14 (2020).
5. H. K. Long, S. L. Prescott, J. Wysocka, Ever-Changing Landscapes: Transcriptional Enhancers in Development and Evolution. *Cell*. **167**, 1170–1187 (2016).
6. D. Villar, C. Berthelot, S. Aldridge, T. F. Rayner, M. Lukk, M. Pignatelli, T. J. Park, R. Deaville, J. T. Erichsen, A. J. Jasinska, J. M. A. Turner, M. F. Bertelsen, E. P. Murchison, P. Flicek, D. T. Odom, Enhancer evolution across 20 mammalian species. *Cell*. **160**, 554–566 (2015).
7. C. Berthelot, D. Villar, J. E. Horvath, D. T. Odom, P. Flicek, Complexity and conservation of regulatory landscapes underlie evolutionary resilience of mammalian gene expression. *Nat. Ecol. Evol.* **2**, 152–163 (2018).
8. S. K. Reilly, J. Yin, A. E. Ayoub, D. Emera, J. Leng, J. Cotney, R. Sarro, P. Rakic, J. P. Noonan, Evolutionary changes in promoter and enhancer activity during human corticogenesis. *Science.* **347**, 1155–1159 (2015).
9. G. Bejerano, M. Pheasant, I. Makunin, S. Stephen, W. J. Kent, J. S. Mattick, D. Haussler, Ultraconserved elements in the human genome. *Science.* **304**, 1321–1325 (2004).
10. D. E. Dickel, A. R. Ypsilanti, R. Pla, Y. Zhu, I. Barozzi, B. J. Mannion, Y. S. Khin, Y. Fukuda-Yuzawa, I. Plajzer-Frick, C. S. Pickle, E. A. Lee, A. N. Harrington, Q. T. Pham, T. H. Garvin, M. Kato, M. Osterwalder, J. A. Akiyama, V. Afzal, J. L. R. Rubenstein, L. A. Pennacchio, A. Visel, Ultraconserved Enhancers Are Required for Normal Development. *Cell*. **172**, 491-499.e15 (2018).
11. D. U. Gorkin, I. Barozzi, Y. Zhao, Y. Zhang, H. Huang, A. Y. Lee, B. Li, J. Chiou, A. Wildberg, B. Ding, B. Zhang, M. Wang, J. S. Strattan, J. M. Davidson, Y. Qiu, V. Afzal, J. A. Akiyama, I. Plajzer-Frick, C. S. Novak, M. Kato, T. H. Garvin, Q. T. Pham, A. N. Harrington, B. J. Mannion, E. A. Lee, Y. Fukuda-Yuzawa, Y. He, S. Preissl, S. Chee, J. Y. Han, B. A. Williams, D. Trout, H. Amrhein, H. Yang, J. M. Cherry, W. Wang, K. Gaulton, J. R. Ecker, Y. Shen, D. E. Dickel, A. Visel, L. A. Pennacchio, B. Ren, An atlas of dynamic chromatin landscapes in mouse fetal development. *Nature*. **583**, 744–751 (2020).

12. C. L. Frank, F. Liu, R. Wijayatunge, L. Song, M. T. Biegler, M. G. Yang, C. M. Vockley, A. Safi, C. A. Gersbach, G. E. Crawford, A. E. West, Regulation of chromatin accessibility and Zic binding at enhancers in the developing cerebellum. *Nat. Neurosci.* **18**, 647–656 (2015).

13. A. S. Nord, M. J. Blow, C. Attanasio, J. A. Akiyama, A. Holt, R. Hosseini, S. Phouanenavong, I. Plajzer-Frick, M. Shoukry, V. Afzal, J. L. R. Rubenstein, E. M. Rubin, L. A. Pennacchio, A. Visel, Rapid and pervasive changes in genome-wide enhancer usage during mammalian development. *Cell*. **155**, 1521–1531 (2013).

14. A. B. Stergachis, S. Neph, A. Reynolds, R. Humbert, B. Miller, S. L. Paige, B. Vernot, J. B. Cheng, R. E. Thurman, R. Sandstrom, E. Haugen, S. Heimfeld, C. E. Murry, J. M. Akey, J. A. Stamatoyannopoulos, Developmental fate and cellular maturity encoded in human regulatory DNA landscapes. *Cell*. **154**, 888–903 (2013).

15. D. A. Cusanovich, A. J. Hill, D. Aghamirzaie, R. M. Daza, H. A. Pliner, J. B. Berletch, G. N. Filippova, X. Huang, L. Christiansen, W. S. DeWitt, C. Lee, S. G. Regalado, D. F. Read, F. J. Steemers, C. M. Disteche, C. Trapnell, J. Shendure, A Single-Cell Atlas of In Vivo Mammalian Chromatin Accessibility. *Cell*. **174**, 1309-1324.e18 (2018).

16. Y. E. Li, S. Preissl, X. Hou, Z. Zhang, K. Zhang, R. Fang, Y. Qiu, O. Poirion, B. Li, H. Liu, X. Wang, J. Y. Han, J. Lucero, Y. Yan, S. Kuan, D. Gorkin, M. Nunn, E. Mukamel, M. M. Behrens, J. Ecker, B. Ren, An Atlas of Gene Regulatory Elements in Adult Mouse Cerebrum. *bioRxiv* (2020)*,* doi:10.1101/2020.05.10.087585.

17. S. Preissl, R. Fang, H. Huang, Y. Zhao, R. Raviram, D. U. Gorkin, Y. Zhang, B. C. Sos, V. Afzal, D. E. Dickel, S. Kuan, A. Visel, L. A. Pennacchio, K. Zhang, B. Ren, Single-nucleus analysis of accessible chromatin in developing mouse forebrain reveals cell-type-specific transcriptional regulation. *Nat. Neurosci.* **21**, 432–439 (2018).

18. D. J. Di Bella, E. Habibi, R. R. Stickels, G. Scalia, J. Brown, P. Yadollahpour, S. M. Yang, C. Abbate, T. Biancalani, E. Z. Macosko, F. Chen, A. Regev, P. Arlotta, Molecular logic of cellular diversification in the mouse cerebral cortex. *Nature*, in press, (2021), doi:10.1038/s41586-021-03670-5.

19. R. S. Ziffra, C. N. Kim, A. Wilfert, T. N. Turner, M. Haeussler, A. M. Casella, P. F. Przytycki, A. Kreimer, K. S. Pollard, S. A. Ament, E. E. Eichler, N. Ahituv, T. J. Nowakowski, Single cell epigenomic atlas of the developing human brain and organoids. *bioRxiv* (2019), doi:10.1101/2019.12.30.891549.

20. S. Domcke, A. J. Hill, R. M. Daza, J. Cao, D. R. O'Day, H. A. Pliner, K. A. Aldinger, D. Pokholok, F. Zhang, J. H. Milbank, M. A. Zager, I. A. Glass, F. J. Steemers, D. Doherty, C. Trapnell, D. A. Cusanovich, J. Shendure, A human cell atlas of fetal chromatin accessibility. *Science.* **370**, eaba7612 (2020).

21. A. T. Satpathy, J. M. Granja, K. E. Yost, Y. Qi, F. Meschi, G. P. McDermott, B. N. Olsen, M. R. Mumbach, S. E. Pierce, M. R. Corces, P. Shah, J. C. Bell, D. Jhutty, C. M. Nemec, J. Wang, L. Wang, Y. Yin, P. G. Giresi, A. L. S. Chang, G. X. Y. Zheng, W. J. Greenleaf, H. Y. Chang, Massively parallel single-cell chromatin landscapes of human immune cell development and intratumoral T cell exhaustion. *Nat. Biotechnol.* **37**, 925–936 (2019).

22. J. M. Granja, M. R. Corces, S. E. Pierce, S. T. Bagdatli, H. Choudhry, H. Y. Chang, W. J.

Greenleaf, ArchR is a scalable software package for integrative single-cell chromatin accessibility analysis. *Nat. Genet.* **53**, 403–411 (2021).

23. M. C. Vladoiu, I. El-Hamamy, L. K. Donovan, H. Farooq, B. L. Holgado, Y. Sundaravadanam, V. Ramaswamy, L. D. Hendrikse, S. Kumar, S. C. Mack, J. J. Y. Y. Lee, V. Fong, K. Juraschka, D. Przelicki, A. Michealraj, P. Skowron, B. Luu, H. Suzuki, A. S. Morrissy, F. M. G. G. Cavalli, L. Garzia, C. Daniels, X. Wu, M. A. Qazi, S. K. Singh, J. A. Chan, M. A. Marra, D. Malkin, P. Dirks, L. Heisler, T. Pugh, K. Ng, F. Notta, E. M. Thompson, C. L. Kleinman, A. L. Joyner, N. Jabado, L. Stein, M. D. Taylor, Childhood cerebellar tumours mirror conserved fetal transcriptional programs. *Nature*. **572**, 67–73 (2019).

24. J. W. Wizeman, Q. Guo, E. M. Wilion, J. Y. H. Li, Specification of diverse cell types during early neurogenesis of the mouse cerebellum. *Elife*. **8**, 1–24 (2019).

25. K. J. Millen, E. Y. Steshina, I. Y. Iskusnykh, V. V. Chizhikov, Transformation of the cerebellum into more ventral brainstem fates causes cerebellar agenesis in the absence of Ptf1a function. *Proc. Natl. Acad. Sci.* **111**, E1777–E1786 (2014).

26. A. Kriegstein, A. Alvarez-Buylla, The glial nature of embryonic and adult neural stem cells. *Annu. Rev. Neurosci.* **32**, 149–184 (2009).

27. R. A. Carter, L. Bihannic, C. Rosencrance, J. L. Hadley, Y. Tong, T. N. Phoenix, S. Natarajan, J. Easton, P. A. Northcott, C. Gawad, A Single-Cell Transcriptional Atlas of the Developing Murine Cerebellum. *Curr. Biol.* **28**, 2910-2920.e2 (2018).

28. A. Visel, S. Minovitsky, I. Dubchak, L. A. Pennacchio, VISTA Enhancer Browser - A database of tissue-specific human enhancers. *Nucleic Acids Res.* **35**, D88–D92 (2007).

29. M. Dalby, S. Rennie, R. Andersson, FANTOM5 transcribed enhancers in mm10 [Data set] (2018), (available at http://doi.org/10.5281/zenodo.1411211).

30. B. Bonev, N. Mendelson Cohen, Q. Szabo, L. Fritsch, G. L. Papadopoulos, Y. Lubling, X. Xu, X. Lv, J. P. Hugnot, A. Tanay, G. Cavalli, Multiscale 3D Genome Rewiring during Mouse Neural Development. *Cell*. **171**, 557-572.e24 (2017).

31. G. Sabarís, I. Laiker, E. Preger-Ben Noon, N. Frankel, Actors with Multiple Roles: Pleiotropic Enhancers and the Paradigm of Enhancer Modularity. *Trends Genet.* **35**, 423–433 (2019).

32. W. Meuleman, A. Muratov, E. Rynes, J. Halow, K. Lee, D. Bates, M. Diegel, D. Dunn, F. Neri, A. Teodosiadis, A. Reynolds, E. Haugen, J. Nelson, A. Johnson, M. Frerker, M. Buckley, R. Sandstrom, J. Vierstra, R. Kaul, J. Stamatoyannopoulos, Index and biological spectrum of human DNase I hypersensitive sites. *Nature*. **584**, 244–251 (2020).

33. A. Sagner, I. Zhang, T. Watson, J. Lazaro, M. Melchionda, J. Briscoe, Temporal patterning of the central nervous system by a shared transcription factor code. *bioRxiv* (2020), doi:https://doi.org/10.1101/2020.11.10.376491.

34. T. Zhang, T. Liu, N. Mora, J. Guegan, M. Bertrand, X. Contreras, A. H. Hansen, C. Streicher, M. Anderle, N. Danda, L. Tiberi, S. Hippenmeyer, B. A. Hassan, Generation of excitatory and inhibitory neurons from common progenitors via Notch signaling in the cerebellum. *Cell Rep.* **35**, 109208 (2021).

35. Y. Seto, T. Nakatani, N. Masuyama, S. Taya, M. Kumai, Y. Minaki, A. Hamaguchi, Y. U. Inoue, T. Inoue, S. Miyashita, T. Fujiyama, M. Yamada, H. Chapman, K. Campbell, M. A. Magnuson, C. V. Wright, Y. Kawaguchi, K. Ikenaka, H. Takebayashi, S. Ishiwata, Y. Ono, M. Hoshino, Temporal identity transition from Purkinje cell progenitors to GABAergic interneuron progenitors in the cerebellum. *Nat. Commun.* **5**, 3337 (2014).

36. V. Cerrato, E. Parmigiani, M. Figueres-Oñate, M. Betizeau, J. Aprato, I. Nanavaty, P. Berchialla, F. Luzzati, C. De'Sperati, L. López-Mascaraque, A. Buffo, Multiple origins and modularity in the spatiotemporal emergence of cerebellar astrocyte heterogeneity. *PLoS Biol.* **16**, 1–38 (2018).

37. V. Kozareva, C. Martin, T. Osorno, S. Rudolph, C. Guo, C. Vanderburg, N. Nadaf, A. Regev, W. Regehr, E. Macosko, A transcriptomic atlas of the mouse cerebellum reveals regional specializations and novel cell types. *bioRxiv* (2020), doi:10.1101/2020.03.04.976407.

38. L. Telley, G. Agirman, J. Prados, N. Amberg, S. Fièvre, P. Oberst, G. Bartolini, I. Vitali, C. Cadilhac, S. Hippenmeyer, L. Nguyen, A. Dayer, D. Jabaudon, Temporal patterning of apical progenitors and their daughter neurons in the developing neocortex. *Science.* **364**, eaav2522 (2019).

39. M. Cardoso-Moreira, J. Halbert, D. Valloton, B. Velten, C. Chen, Y. Shao, A. Liechti, K. Ascenção, C. Rummel, S. Ovchinnikova, P. V. Mazin, I. Xenarios, K. Harshman, M. Mort, D. N. Cooper, C. Sandi, M. J. Soares, P. G. Ferreira, S. Afonso, M. Carneiro, J. M. A. Turner, J. L. VandeBerg, A. Fallahshahroudi, P. Jensen, R. Behr, S. Lisgo, S. Lindsay, P. Khaitovich, W. Huber, J. Baker, S. Anders, Y. E. Zhang, H. Kaessmann, Gene expression across mammalian organ development. *Nature*. **571**, 505–509 (2019).

40. I. Sarropoulos, R. Marin, M. Cardoso-Moreira, H. Kaessmann, Developmental dynamics of lncRNAs across mammalian organs and species. *Nature*. **571**, 510–514 (2019).

41. A. Siepel, G. Bejerano, J. S. Pedersen, A. S. Hinrichs, M. Hou, K. Rosenbloom, H. Clawson, J. Spieth, L. D. W. Hillier, S. Richards, G. M. Weinstock, R. K. Wilson, R. A. Gibbs, W. J. Kent, W. Miller, D. Haussler, Evolutionarily conserved elements in vertebrate, insect, worm, and yeast genomes. *Genome Res.* **15**, 1034–1050 (2005).

42. D. Arendt, J. M. Musser, C. V. H. Baker, A. Bergman, C. Cepko, D. H. Erwin, M. Pavlicev, G. Schlosser, S. Widder, M. D. Laubichler, G. P. Wagner, The origin and evolution of cell types. *Nat. Rev. Genet.* **17**, 744–757 (2016).

43. M. Roller, E. Stamper, D. Villar, O. Izuogu, F. Martin, A. M. Redmond, R. Ramachanderan, L. Harewood, D. T. Odom, P. Flicek, LINE retrotransposons characterize mammalian tissue-specific and evolutionarily dynamic regulatory regions. *Genome Biol.* **22**, 62 (2021).

44. L. Geirsdottir, E. David, H. Keren-Shaul, A. Weiner, S. C. Bohlen, J. Neuber, A. Balic, A. Giladi, F. Sheban, C. A. Dutertre, C. Pfeifle, F. Peri, A. Raffo-Romero, J. Vizioli, K. Matiasek, C. Scheiwe, S. Meckel, K. Mätz-Rensing, F. van der Meer, F. R. Thormodsson, C. Stadelmann, N. Zilkha, T. Kimchi, F. Ginhoux, I. Ulitsky, D. Erny, I. Amit, M. Prinz, Cross-Species Single-Cell Analysis Reveals Divergence of the Primate Microglia Program. *Cell*. **179**, 1609-1622.e16 (2019).

45. D. Brawand, M. Soumillon, A. Necsulea, P. Julien, G. Csárdi, P. Harrigan, M. Weier, A. Liechti, A. Aximu-Petri, M. Kircher, F. W. Albert, U. Zeller, P. Khaitovich, F. Grützner, S. Bergmann, R. Nielsen, S. Pääbo, H. Kaessmann, The evolution of gene expression levels in mammalian organs. *Nature*. **478**, 343–348 (2011).

46. A. Iulianella, R. J. Wingate, C. B. Moens, E. Capaldo, The generation of granule cells during the development and evolution of the cerebellum. *Dev. Dyn.* **248**, 506–513 (2019).

47. M. Götz, S. Sirko, J. Beckers, M. Irmler, Reactive astrocytes as neural stem or progenitor cells: In vivo lineage, In vitro potential, and Genome-wide expression analysis. *Glia*. **63**, 1452–1468 (2015).

48. A. Volterra, J. Meldolesi, Astrocytes, from brain glue to communication elements: The revolution continues. *Nat. Rev. Neurosci.* **6**, 626–640 (2005).

49. Allen Institute for Brain Science, Allen Developing Mouse Brain Atlas (2008), (available at http://developingmouse.brain-map.org/).

50. I. Korsunsky, N. Millard, J. Fan, K. Slowikowski, F. Zhang, K. Wei, Y. Baglaenko, M. Brenner, P. ru Loh, S. Raychaudhuri, Fast, sensitive and accurate integration of single-cell data with Harmony. *Nat. Methods*. **16**, 1289–1296 (2019).

51. L. Haghverdi, M. Büttner, F. A. Wolf, F. Buettner, F. J. Theis, Diffusion pseudotime robustly reconstructs lineage branching. *Nat. Methods*. **13**, 845–848 (2016).

52. S. R. Krishnaswami, R. V Grindberg, M. Novotny, P. Venepally, B. Lacar, K. Bhutani, S. B. Linker, S. Pham, J. A. Erwin, J. A. Miller, R. Hodge, J. K. McCarthy, M. Kelder, J. McCorrison, B. D. Aevermann, F. D. Fuertes, R. H. Scheuermann, J. Lee, E. S. Lein, N. Schork, M. J. McConnell, F. H. Gage, R. S. Lasken, Using single nuclei for RNA-seq to capture the transcriptome of postmortem neurons. *Nat. Protoc.* **11**, 499–524 (2016).

53. T. Stuart, A. Butler, P. Hoffman, C. Hafemeister, E. Papalexi, W. M. Mauck, Y. Hao, M. Stoeckius, P. Smibert, R. Satija, Comprehensive Integration of Single-Cell Data. *Cell*. **177**, 1888-1902.e21 (2019).

54. Y. Zhang, T. Liu, C. A. Meyer, J. Eeckhoute, D. S. Johnson, B. E. Bernstein, C. Nussbaum, R. M. Myers, M. Brown, W. Li, X. S. Liu, Model-based Analysis of ChIP-Seq (MACS). *Genome Biol.* **9**, R137 (2008).

55. M. Haeussler, A. S. Zweig, C. Tyner, M. L. Speir, K. R. Rosenbloom, B. J. Raney, C. M. Lee, B. T. Lee, A. S. Hinrichs, J. N. Gonzalez, D. Gibson, M. Diekhans, H. Clawson, J. Casper, G. P. Barber, D. Haussler, R. M. Kuhn, W. J. Kent, The UCSC Genome Browser database: 2019 update. *Nucleic Acids Res.* **47**, D853–D858 (2019).

56. F. Cunningham, P. Achuthan, W. Akanni, J. Allen, M. R. Amode, I. M. Armean, R. Bennett, J. Bhai, K. Billis, S. Boddu, C. Cummins, C. Davidson, K. J. Dodiya, A. Gall, C. G. Girón, L. Gil, T. Grego, L. Haggerty, E. Haskell, T. Hourlier, O. G. Izuogu, S. H. Janacek, T. Juettemann, M. Kay, M. R. Laird, I. Lavidas, Z. Liu, J. E. Loveland, J. C. Marugán, T. Maurel, A. C. McMahon, B. Moore, J. Morales, J. M. Mudge, M. Nuhn, D. Ogeh, A. Parker, A. Parton, M. Patricio, A. I. Abdul Salam, B. M. Schmitt, H. Schuilenburg, D. Sheppard, H. Sparrow, E. Stapleton, M. Szuba, K. Taylor, G. Threadgold, A. Thormann, A. Vullo, B. Walts, A. Winterbottom, A. Zadissa, M. Chakiachvili, A. Frankish, S. E. Hunt, M. Kostadima, N. Langridge, F. J. Martin, M.

Muffato, E. Perry, M. Ruffier, D. M. Staines, S. J. Trevanion, B. L. Aken, A. D. Yates, D. R. Zerbino, P. Flicek, Ensembl 2019. *Nucleic Acids Res.* **47**, D745–D751 (2019).

57. A. R. Quinlan, I. M. Hall, BEDTools: A flexible suite of utilities for comparing genomic features. *Bioinformatics*. **26**, 841–842 (2010).

58. A. N. Schep, B. Wu, J. D. Buenrostro, W. J. Greenleaf, ChromVAR: Inferring transcription-factor-associated accessibility from single-cell epigenomic data. *Nat. Methods*. **14**, 975–978 (2017).

59. M. T. Weirauch, A. Yang, M. Albu, A. G. Cote, A. Montenegro-Montero, P. Drewe, H. S. Najafabadi, S. A. Lambert, I. Mann, K. Cook, H. Zheng, A. Goity, H. van Bakel, J. C. Lozano, M. Galli, M. G. Lewsey, E. Huang, T. Mukherjee, X. Chen, J. S. Reece-Hoyes, S. Govindarajan, G. Shaulsky, A. J. M. Walhout, F. Y. Bouget, G. Ratsch, L. F. Larrondo, J. R. Ecker, T. R. Hughes, Determination and inference of eukaryotic transcription factor sequence specificity. *Cell*. **158**, 1431–1443 (2014).

60. W. J. Kent, A. S. Zweig, G. Barber, A. S. Hinrichs, D. Karolchik, BigWig and BigBed: Enabling browsing of large distributed datasets. *Bioinformatics*. **26**, 2204–2207 (2010).

61. D. Karolchik, The UCSC Table Browser data retrieval tool. *Nucleic Acids Res.* **32**, 493D – 496 (2004).

62. M. L. Delignette-Muller, C. Dutang, fitdistrplus: An R package for fitting distributions. *J. Stat. Softw.* **64**, 1–34 (2015).

63. M. D. Robinson, D. J. McCarthy, G. K. Smyth, edgeR: A Bioconductor package for differential expression analysis of digital gene expression data. *Bioinformatics*. **26**, 139–140 (2009).

64. A. E. Trevino, N. Sinnott-Armstrong, J. Andersen, S. Yoon, N. Huber, J. K. Pritchard, H. Y. Chang, W. J. Greenleaf, S. P. Pașca, Chromatin accessibility dynamics in a model of human forebrain development. *Science.* **367**, eaay1645 (2020).

65. M. I. Love, W. Huber, S. Anders, Moderated estimation of fold change and dispersion for RNA-seq data with DESeq2. *Genome Biol.* **15**, 550 (2014).

66. C. Y. McLean, D. Bristor, M. Hiller, S. L. Clarke, B. T. Schaar, C. B. Lowe, A. M. Wenger, G. Bejerano, GREAT improves functional interpretation of cis-regulatory regions. *Nat. Biotechnol.* **28**, 495–501 (2010).

67. S. Heinz, C. Benner, N. Spann, E. Bertolino, Y. C. Lin, P. Laslo, J. X. Cheng, C. Murre, H. Singh, C. K. Glass, Simple Combinations of Lineage-Determining Transcription Factors Prime cis-Regulatory Elements Required for Macrophage and B Cell Identities. *Mol. Cell*. **38**, 576–589 (2010).

68. F. Supek, M. Bošnjak, N. Škunca, T. Šmuc, REVIGO Summarizes and Visualizes Long Lists of Gene Ontology Terms. *PLoS One*. **6**, e21800 (2011).

69. R. Suzuki, Y. Terada, H. Shimodaira, pvclust: Hierarchical Clustering with P-Values via Multiscale Bootstrap Resampling. (2019), (available at https://cran.r-project.org/package=pvclust).

70. M. E. Futschik, L. Kumar, M. E Futschik, Introduction to Mfuzz package and its graphical

user interface. *Analysis*, 1–13 (2009).

71. F. A. Wolf, P. Angerer, F. J. Theis, SCANPY: Large-scale single-cell gene expression data analysis. *Genome Biol.* **19**, 15 (2018).

72. C. Pardy, mpmi: Mixed-Pair Mutual Information Estimators. (2019), (available at https://cran.r-project.org/package=mpmi).

73. L. Scrucca, M. Fop, T. B. Murphy, A. E. Raftery, Mclust 5: Clustering, classification and density estimation using Gaussian finite mixture models. *R J.* **8**, 289–317 (2016).

74. Z. Gu, L. Gu, R. Eils, M. Schlesner, B. Brors, Circlize implements and enhances circular visualization in R. *Bioinformatics*. **30**, 2811–2812 (2014).

75. S. Lê, J. Josse, F. Husson, FactoMineR: An R package for multivariate analysis. *J. Stat. Softw.* **25**, 1–18 (2008).

76. I. Berest, C. Arnold, A. Reyes-Palomares, G. Palla, K. D. Rasmussen, H. Giles, P. M. Bruch, W. Huber, S. Dietrich, K. Helin, J. B. Zaugg, Quantification of Differential Transcription Factor Activity and Multiomics-Based Classification into Activators and Repressors: diffTF. *Cell Rep.* **29**, 3147-3159.e12 (2019).

77. H. Hu, Y. R. Miao, L. H. Jia, Q. Y. Yu, Q. Zhang, A. Y. Guo, AnimalTFDB 3.0: A comprehensive resource for annotation and prediction of animal transcription factors. *Nucleic Acids Res.* **47**, D33–D38 (2019).

78. A. Conesa, M. J. Nueda, A. Ferrer, M. Talón, maSigPro: A method to identify significantly differential expression profiles in time-course microarray experiments. *Bioinformatics*. **22**, 1096–1102 (2006).

79. R Core Team, R: A Language and Environment for Statistical Computing (2020), (available at https://www.r-project.org/).

80. H. Wickham, M. Averick, J. Bryan, W. Chang, L. McGowan, R. François, G. Grolemund, A. Hayes, L. Henry, J. Hester, M. Kuhn, T. Pedersen, E. Miller, S. Bache, K. Müller, J. Ooms, D. Robinson, D. Seidel, V. Spinu, K. Takahashi, D. Vaughan, C. Wilke, K. Woo, H. Yutani, Welcome to the Tidyverse. *J. Open Source Softw.* **4**, 1686 (2019).

81. M. Dowle, A. Srinivasan, data.table: Extension of `data.frame` (2017).

82. D. Bates, M. Maechler, Matrix: Sparse and Dense Matrix Classes and Methods (2019).

83. M. Morgan, V. Obenchain, J. Hester, H. Pagès, SummarizedExperiment: SummarizedExperiment container (2019).

84. J. Baglama, L. Reichel, B. W. Lewis, irlba: Fast Truncated Singular Value Decomposition and Principal Components Analysis for Large Dense and Sparse Matrices (2019), (available at https://cran.r-project.org/package=irlba).

85. M. Maechler, P. Rousseeuw, A. Struyf, M. Hubert, K. Hornik, cluster: Cluster Analysis Basics and Extensions. (2019).

86. Z. Gu, R. Eils, M. Schlesner, Complex heatmaps reveal patterns and correlations in multidimensional genomic data. *Bioinformatics*. **32**, 2847–2849 (2016).

87. R. Kolde, pheatmap: Pretty Heatmaps. (2019), (available at https://cran.r-

project.org/package=pheatmap).

88. W. Chang, J. Cheng, J. Allaire, Y. Xie, J. McPherson, shiny: Web Application Framework for R (2020).

89. D. Attali, shinyjs: Easily Improve the User Experience of Your Shiny Apps in Seconds (2020), (available at https://cran.r-project.org/package=shinyjs).

90. F. Hahne, R. Ivanek, Visualizing Genomic Data Using Gviz and Bioconductor. *Methods Mol. Biol.* **1418**, 335–351 (2016).

91. N. Harmston, E. Ing-Simmons, M. Perry, A. Baresic, B. Lenhard, GenomicInteractions: R package for handling genomic interaction data (2020), (available at https://www.bioconductor.org/packages/release/bioc/html/GenomicInteractions.html).

92. H. T. Prekop, A. Kroiss, V. Rook, L. Zagoraiou, T. M. Jessell, C. Fernandes, A. Delogu, R. J. T. Wingate, Sox14 is required for a specific subset of cerebello–olivary projections. *J. Neurosci.* **38**, 9539–9550 (2018).

93. V. V. Chizhikov, A. G. Lindgren, Y. Mishima, R. W. Roberts, K. A. Aldinger, G. R. Miesegaes, D. Spencer Currle, E. S. Monuki, K. J. Millen, Lmx1a regulates fates and location of cells originating from the cerebellar rhombic lip and telencephalic cortical hem. *Proc. Natl. Acad. Sci. U. S. A.* **107**, 10725–10730 (2010).